

Solar Neutrinos: Status and Prospects

W. C. HAXTON

*Department of Physics, University of California, Berkeley, and Nuclear Science
Division, Lawrence Berkeley National Laboratory, Berkeley CA 94720-7300*

R. G. HAMISH ROBERTSON

*Department of Physics, University of Washington, and Center for Experimental
Nuclear Physics and Astrophysics, Seattle, WA 98195*

ALDO M. SERENELLI

*Instituto de Ciencias del Espacio (CSIC-IEEC), Facultad de Ciencias, Campus
UAB, 08193 Bellaterra, Spain and Max Planck Institute for Astrophysics, Karl
Schwarzschild Str. 1, Garching, D-85471, Germany*

Key Words solar neutrinos, neutrino oscillations, solar models, helioseismol-
ogy, nuclear astrophysics, metal abundances

Abstract We describe the current status of solar neutrino measurements and of the theory – both neutrino physics and solar astrophysics – employed in interpreting measurements. Important recent developments include Super-Kamiokande’s determination of the $\nu - e$ elastic scattering rate for ^8B neutrinos to 3%; the latest SNO global analysis in which the inclusion of

low-energy data from SNO I and II significantly narrowed the range of allowed values for the neutrino mixing angle θ_{12} ; Borexino results for both the ${}^7\text{Be}$ and pep neutrino fluxes, the first direct measurements constraining the rate of ppI and ppII burning in the Sun; global reanalyses of solar neutrino data that take into account new reactor results on θ_{13} ; a new decadal evaluation of the nuclear physics of the pp chain and CNO cycle defining best values and uncertainties in the nuclear microphysics input to solar models; recognition of an emerging discrepancy between two tests of solar metallicity, helioseismological mappings of the sound speed in the solar interior, and analyses of the metal photoabsorption lines based on our best current description of the Sun's photosphere; a new round of standard solar model calculations optimized to agree either with helioseismology or with the new photospheric analysis; and, motivated by the solar abundance problem, the development of nonstandard, accreting solar models, in order to investigate possible consequences of the metal segregation that occurred in the proto-solar disk. We review this progress and describe how new experiments such as SNO+ could help us further exploit neutrinos as a unique probe of stellar interiors.

CONTENTS

INTRODUCTION	3
THE SSM AND ITS NUCLEAR AND NEUTRINO PHYSICS	8
<i>The Standard Solar Model</i>	8
<i>The pp Chain and CN cycle</i>	11
<i>Solar Neutrino Fluxes</i>	14
EXPERIMENTS: NEUTRINOS AND HELIOSEISMOLOGY	17
<i>Neutrino Spectroscopy: Early Experiments</i>	18
<i>Helioseismology</i>	25
<i>Super-Kamiokande</i>	28
<i>Sudbury Neutrino Observatory</i>	30
<i>Borexino</i>	33
NEW NEUTRINO PROPERTIES	34

<i>Oscillation Basics: The Vacuum Case</i>	36
<i>Oscillation Basics: Matter and the MSW Mechanism</i>	38
GLOBAL ANALYSES AND NEUTRINO PROPERTIES	41
<i>Vacuum Mixing Angles and Mass² Differences</i>	42
<i>Spectral Distortions: LET Analyses and Borexino</i>	45
<i>Day-Night Differences</i>	46
NEUTRINO CONSTRAINTS ON SOLAR STRUCTURE	48
<i>The Solar Abundance Problem and its SSM Implications</i>	49
<i>Solar Models with Accretion</i>	52
<i>Neutrinos as a Direct Probe of Solar Composition: SNO+</i>	56
OUTLOOK AND CHALLENGES	59
LITERATURE CITED	62

1 INTRODUCTION

In 1958 Holmgren & Johnston (1958, 1959) found that the cross section for ${}^3\text{He} + {}^4\text{He} \rightarrow {}^7\text{Be} + \gamma$ was about 1000 times larger than anticipated, so that in addition to the simplest ${}^3\text{He} + {}^3\text{He} \rightarrow {}^4\text{He} + 2\text{p}$ ppI termination of the pp chain (see Fig. 1), there might be significant branches to the ppII and ppIII cycles, and thus significant fluxes of ${}^7\text{Be}$ and ${}^8\text{B}$ solar neutrinos. Despite the uncertainties that existed in 1958 – the solar core temperature was poorly constrained by theory, and other nuclear physics important to the pp chain had not been resolved – both Cameron (1958) and Fowler (1958) pointed out that it might therefore be possible to detect solar neutrinos using a radiochemical method Ray Davis had developed at Brookhaven (Davis Jr. 1955). While the endpoint of the main source of neutrinos from the ppI cycle, $\text{p} + \text{p} \rightarrow \text{d} + \text{e}^+ + \nu_e$, is below the 811 keV threshold

for $\nu_e + {}^{37}\text{Cl} \rightarrow {}^{37}\text{Ar} + e^-$, most ${}^7\text{Be}$ and ${}^8\text{B}$ neutrinos are sufficiently energetic to drive this reaction. In 1962 Fowler organized a team of young Caltech researchers – John Bahcall, Icko Iben, and Dick Sears – to begin the development of a solar model to more accurately predict the central temperature of the Sun and to estimate the rates of neutrino-producing reactions (Bahcall et al. 1963). The history of these early developments is summarized in several sources (Bahcall & Davis Jr. 1982, Haxton 2010, Lande 2010). By early 1964, following significant advances in the solar model and in the understanding of the nuclear physics of the pp chain and the ${}^{37}\text{Cl}(\nu_e, e^-){}^{37}\text{Ar}$ reaction, Davis Jr. (1964) and Bahcall (1964) concluded that a measurement of solar neutrinos would be possible, were Davis to mount a detector 100 times larger than that he built at Brookhaven, in a site sufficiently deep to reduce backgrounds from high-energy cosmic ray muons to an acceptable level. In April 1968 Davis Jr., Harmer & Hoffman (1968) announced an upper bound on the solar neutrino capture rate for ${}^{37}\text{Cl}$ of 3 SNU (1 SNU = 10^{-36} captures/target atom/s), based on the initial running of a 100,000-gallon C_2Cl_4 detector that the collaborators had constructed on the 4850-ft level of the Homestake gold mine, in Lead, South Dakota.

This upper bound, nearly a factor of three below the rate predicted by the Bahcall, Bahcall & Shaviv (1968) standard solar model (SSM), began a controversy that took 30 years to resolve. Twenty of these years passed without independent confirmation of the Davis result: as the Cl rate was a fraction of a count per day in 0.6 kilotons of organic liquid, other technologies with comparable sensitivity were not easily developed. Because the Davis experiment was sensitive to a flux of neutrinos that varies sharply with the solar core temperature ($\phi({}^8\text{B}) \sim T_C^{22}$ (Bahcall 1989)), the result could be accommodated by a variety of possible

changes in the SSM having the net effect of reducing T_C by $\sim 5\%$. But as additional constraints on solar neutrino fluxes were established by the Kamiokande (Kamiokande Collaboration, K. S. Hirata et al. 1989), SAGE (SAGE Collaboration, J. N. Abdurashitov et al. 1994), and GALLEX (GALLEX Collaboration, P. Anselmann et al. 1994) collaborations, a more detailed pattern of fluxes emerged that was not easily reconciled with the SSM. In contrast, with the discovery of the MSW mechanism (Mikheyev & Smirnov 1985, 1986, Wolfenstein 1978a,b), it became apparent that neutrino oscillations augmented by matter effects could account for the observations, even for a small mixing angle. The conclusions of an Annual Reviews article from this period (Haxton 1995) captures the sense of excitement that with new experiments, a resolution of the solar neutrino problem was near.

In 1998 $\nu_\mu \rightarrow \nu_\tau$ vacuum neutrino oscillations were discovered through the Super-Kamiokande collaboration's study of the zenith-angle dependence of atmospheric neutrino fluxes (Super-Kamiokande Collaboration, Y. Fukuda et al. 1998). While this result did not directly constrain the ν_e s produced by the Sun, the discovery was a game-changer, confirming a phenomenon originally suggested by Pontecorvo (1967) as a possible explanation for the solar neutrino problem. Finally, the Sudbury Neutrino Observatory (SNO) collaboration (SNO Collaboration, Q. R. Ahmad et al. 2001, 2002) measured both the ν_e and heavy-flavor components of the solar neutrino flux arriving at Earth, utilizing three different detection channels with varying sensitivities to charge and neutral currents. The SNO collaboration measured the electron and heavy flavors components of the ${}^8\text{B}$ solar neutrino flux, found that the total flux of neutrinos (summed over flavors) is in good agreement with the SSM prediction, and determined flavor mixing pa-

rameters that attributed the differential suppression of the pp, ${}^7\text{Be}$, and ${}^8\text{B}$ fluxes deduced from previous experiments to the energy-dependent effects of matter on oscillations.

This review summarizes the basic physics of solar neutrinos, the work that led to the discoveries noted above, and the impact of recent and ongoing solar neutrino experiments on astrophysics and weak interactions, including

- Completion of phase III of the Super-Kamiokande experiment (Super-Kamiokande Collaboration, K. Abe et al. 2011) and preliminary results from Super-Kamiokande IV's low-threshold running (Smy 2012);
- SNO's combined analysis of all three SNO phases (SNO Collaboration, B. Aharmim et al. 2012) and the collaboration's low-energy analysis of the data from SNO I and II (SNO Collaboration, B. Aharmim et al. 2010);
- Borexino's achievement of a 5% measurement of the ${}^7\text{Be}$ flux, an initial result for the pep flux, and a limit on the CN neutrino contribution (Borexino Collaboration, G. Bellini et al. 2011, 2012a); and
- Daya Bay, Reno, and Double Chooz measurements of θ_{13} , impacting global analyses of solar neutrino data (Daya Bay Collaboration, F. P. An et al. 2012; Double Chooz Collaboration, Y. Abe et al. 2012; RENO Collaboration, J. K. Ahn et al. 2012).

In addition, a comprehensive survey of the nuclear physics of the pp chain and CNO cycle has been completed, yielding a new set of best values and uncertainties for the nuclear rates (Adelberger et al. 2011). The sound speed throughout most of the Sun's interior has been extracted from helioseismology to an accuracy $\sim 0.1\%$, providing a stringent check on SSM predictions. More sophisticated

3D models of the solar atmosphere have been developed, significantly improving the agreement between predicted and observed absorption line-shapes and the consistency of abundance determinations from different atomic and molecular lines (Asplund et al. 2009) – but also yielding a photospheric metal abundance $\sim 30\%$ below 1D values, leading to a conflict between SSMs employing the new abundances and solar parameters deduced from helioseismology. The SSM has been updated for the new nuclear reaction rates and alternative metallicities, and nonstandard models have been developed to explore accretion as a possible solution to the “solar abundance problem” (Serenelli et al. 2009; Serenelli, Haxton & Peña-Garay 2011).

For three decades solar neutrino physics was defined by an incomplete knowledge of the neutrino fluxes and shortcomings in our understanding of neutrino flavor physics. We are now starting a new period, where precise spectroscopy of the full spectrum of solar neutrinos is possible, and where a clearer understanding of weak interactions has been obtained from a combination of astrophysical, reactor, and accelerator experiments. On one hand, this returns us to the roots of solar neutrino physics: with weak interaction uncertainties removed, solar neutrinos can be used to probe possible limitations in the SSM – such as uncertainties in the Sun’s initial composition and the absence of *ab initio* treatments of mixing and other three-dimensional physics, including rotation and magnetic fields. On the other hand, the neutrinos coming from the Sun remain important to fundamental physics: the spectral shapes and fluxes of the various sources are known rather precisely, and low-energy neutrinos react with targets rather simply, giving us confidence that we can interpret measurements. Thus this review also considers the continuing role solar neutrinos could play in further constrain-

ing the Pontecorvo-Maki-Nakagawa-Sakata (PMNS) neutrino mass matrix and in probing matter effects and other environmental neutrino phenomena.

2 THE SSM AND ITS NUCLEAR AND NEUTRINO PHYSICS

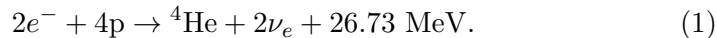
2.1 The Standard Solar Model

Solar models trace the evolution of the Sun from its beginning – when the collapse of the pre-solar gas cloud was halted by the turn-on of thermonuclear reactions – to today, thereby predicting contemporary solar properties such as the composition, temperature, pressure, and sound-speed profiles and the neutrino fluxes. SSMs are based on four assumptions (Bahcall 1989):

- The Sun burns in hydrostatic equilibrium, maintaining a local balance between the gravitation force and pressure gradient. To implement this condition, an equation of state (EoS) is needed. As the hydrogen and helium in the Sun’s core are nearly completely ionized, an ideal gas EoS with corrections for incomplete ionization of metals, radiation pressure, and screening is thought to provide a good approximation to the EoS (Bahcall 1989). Helioseismic inversions of solar p-mode frequencies have provided important tests of our understanding of the associated theory (Elliott & Kosovichev 1998).
- The mechanisms for energy transport are radiation and convection. The inner portion of the Sun – 98% by mass or about 71% by radius – is radiative. In order to describe radiative transport, the opacity must be known as a function of temperature, density, and composition. In addition to elementary processes such Thomson scattering off electrons and inverse brems-

strahlung off fully ionized hydrogen and helium, more complex processes such as bound-free scattering off metals are important contributors to the opacity in the Sun's central regions. Thus modern opacity tables like OPAL (Rogers & Nayfonov 2002) are based on detailed atomic input. Changes in opacity influence important helioseismic properties such as the sound speed and the location of the convective zone boundary. In the Sun's outer envelope, where the radiative gradient is larger, convection dominates the energy transport. SSM convection is modeled through mixing length theory, in which volume elements are transported radially over a characteristic distance determined empirically in the model, but typically on the order of the pressure scale height.

- The Sun produces its energy by fusing protons into ${}^4\text{He}$,



via the pp-chain ($\sim 99\%$) and CN cycle ($\sim 1\%$). The nuclear cross sections are taken from experiment or, if that is impractical, from theory: the associated laboratory astrophysics is challenging because reaction rates are needed for energies well below the Coulomb barrier. Thus laboratory measurements are generally made at higher energies, with theory guiding the extrapolations to the solar Gamow window.

- Boundary conditions include the modern Sun's mass, age, radius R_\odot , and luminosity L_\odot . The pre-solar composition is divided into hydrogen X_{ini} , helium Y_{ini} , and metals Z_{ini} , with $X_{\text{ini}} + Y_{\text{ini}} + Z_{\text{ini}} = 1$. Relative metal abundances can be determined from a combination of photospheric (determined from analyses of absorption lines) and meteoritic (for refractory elements)

abundances, and are generally assumed to have remained constant since the Sun formed. The photospheric abundances and the assumption of a homogeneous zero-age Sun then constrain the Sun’s initial core composition: one can equate the Sun’s pre-solar core metallicity Z_{ini} to its present photospheric Z_S , corrected for the effects of diffusion over the Sun’s lifetime. Finally Y_{ini} and the mixing length α_{MLT} are determined iteratively by demanding that L_{\odot} and R_{\odot} are produced after 4.6 Gy of burning.

The resulting model is dynamic. The luminosity of the Sun increases by $\sim 40\%$ over the solar lifetime: Helium synthesis alters the mean molecular weight and opacity in the core, requiring a response in T_C . The ratio of ppI/ppII/ppIII burning changes, with the fraction of energy produced through the more temperature-sensitive ppII and ppIII branches increasing. The ${}^8\text{B}$ neutrino flux for the ppIII cycle has an exceedingly sharp growth $\sim e^{t/\tau}$ where $\tau \sim 0.9$ Gy. Composition gradients are created as the pp chain burns to equilibrium. An interesting example is the solar core ${}^3\text{He}$ abundance, which rises steeply with increasing radius, $X_3 \propto T^{-6}$, throughout the region where pp-chain equilibrium has been reached. The ${}^3\text{He}$ abundance gradient was proposed as a potential trigger for periodic mixing of the core in the “solar spoon” (Dilke & Gough 1972). Metals are rearranged: in the first 10^8 years of main-sequence burning most of the carbon in the Sun’s central core is converted to nitrogen, building up the core abundance of ${}^{14}\text{N}$. Because they have a smaller charge-to-mass ratio than hydrogen, ${}^4\text{He}$ and metals slowly diffuse toward the core – another source of composition gradients that affect contemporary observables like helioseismology.

Properties of two SSMs we will use in this review are listed in Table 1. The models differ in the values assumed for the photospheric metallicity Z_S , with the

GS98-SFII SSM being more metal rich than the AGSS09-SFII SSM. The table gives the model photospheric helium Y_S and metal Z_S abundances, the radius of the convective zone R_{CZ} , the mean deviation of the sound speed $\langle \delta c/c \rangle$ from the helioseismic profile, the core helium and heavy element abundances Y_C and Z_C , and the Sun's pre-solar abundances Y_{ini} and Z_{ini} .

2.2 The pp Chain and CN cycle

Approximately 80% of the observed stars lie along a path in the Hertzsprung-Russell diagram characterized by energy generation through proton burning. The Sun provides a unique opportunity to test our understanding of such main-sequence stars, as we can compare model predictions to solar properties that are precisely known. This has inspired a great deal of laboratory work to reduce uncertainties in atomic opacities and nuclear cross sections – key SSM input parameters – so that we can assess the reliability of the more fundamental solar physics and weak interactions aspects of the model.

In lower-mass hydrogen-burning stars ${}^4\text{He}$ is synthesized primarily through the pp-chain nuclear reactions shown on the left side of Fig. 1. The rates of the ppI, ppII, and ppIII cycles comprising the pp chain can be determined from the fluxes of the pp/pep, ${}^7\text{Be}$, and ${}^8\text{B}$ neutrinos produced by those cycles. As the relative rates are very sensitive to T_C , the neutrino fluxes are a sensitive thermometer for the solar core, provided the associated nuclear physics is under control.

Rates depend on the quantity $\langle \sigma v \rangle_{\text{MB}}$ where v is the relative velocity between two colliding nuclei, σ is the cross section, and $\langle \rangle_{\text{MB}}$ denotes an average over the Maxwell-Boltzmann relative velocity distribution in the solar plasma. The optimal energy for a solar reaction, called the Gamow peak, is determined from the

competition between a cross section that rises rapidly as the energy climbs the Coulomb barrier, and a relative-velocity distribution that declines rapidly on the Maxwell-Boltzmann tail. Two ppI-cycle reactions, $d+p$ and ${}^3\text{He}+{}^3\text{He}$, have been measured in their Gamow peaks. Data were obtained down to 2.5 and 16 keV, respectively, at LUNA, Gran Sasso's low-background facility for nuclear astrophysics (Bonetti et al. 1999). For other pp-chain reactions, direct measurements are not currently possible because of the severity of the Coulomb suppression. Instead, measurements must be made at higher energies, then extrapolated to solar energies using nuclear models to predict the cross section shape.

Such extrapolations are usually performed by using the S-factor,

$$\sigma(E) = \frac{S(E)}{E} \exp[-2\pi\eta(E)], \quad (2)$$

which removes from the cross section the rapid energy dependence associated with the s-wave interaction of point nuclei. Here the Sommerfeld parameter $\eta(E) = Z_1 Z_2 \alpha/v$, with Z_1 and Z_2 the ion charges, the relative velocity $v = \sqrt{2E/\mu}$, μ is the reduced mass, and α is the fine structure constant ($\hbar = c = 1$). The remaining nuclear physics (including effects of finite nuclear size, higher partial waves, antisymmetrization, and any atomic screening effects not otherwise explicitly treated) is then isolated in $S(E)$, the function used in extrapolations because of its gentler dependence on E . In solar applications $S(E)$ is frequently approximated by its zero-energy value $S(0)$ and corrections determined by its first and second derivatives, $S'(0)$ and $S''(0)$.

The recent review by Adelberger et al. (2011) (Solar Fusion II) details the data and theory issues affecting our understanding of solar cross sections. Uncertain S-factors remain one of the key limitations in SSM neutrino flux predictions. Figure 2 gives the Solar Fusion II summaries for ${}^3\text{He}+{}^3\text{He}\rightarrow{}^4\text{He}+2\text{p}$ (left panel)

and ${}^7\text{Be}+\text{p}\rightarrow{}^8\text{B}+\gamma$ (right panel). While measurements for the first reaction cover the solar energies of interest, the screening environment of a terrestrial target (neutral atoms) differs from that at the center of the Sun (ionized ${}^3\text{He}$). It is apparent from Fig. 2 that the theoretical screening correction is significant.

The reaction ${}^7\text{Be}(\text{p},\gamma){}^8\text{B}$ (right panel of Fig. 2) feeds the ppIII cycle that produces the ${}^8\text{B}$ neutrinos measured by SNO and Super-Kamiokande. This reaction was considered the most uncertain in the pp chain when these detectors began operations, with only a single data set considered sufficiently reliable and well documented for inclusion in an S-factor determination (Adelberger et al. 1998). Four new, high-quality data sets were available for the Solar Fusion II evaluation, yielding $S_{17}(0)=20.8 \pm 0.7$ (expt) ± 1.4 (theor). The dominant error is now the theoretical extrapolation to the Gamow peak.

The CN I cycle, illustrated on the right in Fig. 1, is typically the dominant mode for hydrogen burning in massive main-sequence stars, where core temperatures exceed those of the Sun. Unlike the pp chain, the CN cycle depends on pre-existing metals to catalyze a series of (p, γ) and (p, α) reactions, leading in sum to Eq. (1). Thus the CN cycle is (in most settings) a secondary process, dependent on the star's metallicity. In the Sun the CN cycle converts C to N as it seeks equilibrium. Equilibrium has been reached only in the most central regions of the core, where $T \gtrsim 1.33 \times 10^7\text{K}$. Outside this region, the bottleneck reaction ${}^{14}\text{N}(\text{p},\gamma)$ inhibits cycling. Thus, throughout most of the cooler regions of the core, very little CN-cycle burning takes place: pre-solar ${}^{12}\text{C}$ has already been converted to ${}^{14}\text{N}$, but little ${}^{14}\text{N}$ is being consumed. Still further outward, where $T \lesssim 10^7\text{K}$, the ${}^{12}\text{C}$ lifetime is comparable to the solar age. This is the region in the contemporary Sun where pre-solar ${}^{12}\text{C}$ is being burned. Thus CN-cycle neu-

trinos, produced in the β^+ decay of ^{15}O and ^{13}N , come from two distinct regions. Deep in the solar core equal numbers of ^{15}O and ^{13}N neutrinos are produced in equilibrium burning, while in the distant cool outer regions of the core, only ^{13}N neutrinos are produced.

2.3 Solar Neutrino Fluxes

The main neutrino-producing reactions of the pp chain and CN cycle are summarized in Table 2. Four of the five β decay reactions produce neutrino spectra with allowed shapes and endpoints given by E_ν^{max} . In the fifth, the decay of ^8B , the ^8Be final state is a broad (~ 2 MeV) resonance. As the profile of this resonance is known, the associated small deviations from an allowed spectrum can be calculated. In addition to the main pp/pep, ^7Be , and ^8B neutrinos, a fourth source from a weak side-branch of the pp chain, the hep or $^3\text{He}+\text{p}$ neutrinos, is shown in Fig. 1. These neutrinos are the most energetic produced by the Sun ($E_\nu^{\text{max}} \sim 18.77$ MeV), and thus may be observable in SNO and Super-Kamiokande they populate energy bins above the ^8B neutrino endpoint. The two electron-capture (EC) reactions, $\text{p}+\text{e}^-+\text{p}$ and $^7\text{Be}+\text{e}^-$, produce line sources of neutrinos of energy E_ν^{max} , broadened by thermal effects. There are two lines associated with ^7Be EC, as $\sim 10\%$ of the captures populate the first excited state in ^7Li .

The ppI, ppII, and ppIII contributions to solar energy generation can be determined from measurements of the pp/pep, ^7Be , and ^8B neutrino fluxes. As we will discuss in the next section, the ^7Be and ^8B fluxes are now quite well known, while the first measurement of pep neutrinos was very recently announced. The “solar values” of Table 2 come from the Borexino Collaboration (private communication) which updated an analysis by Bahcall & Peña-Garay (2003), combining

^8B , ^7Be , and pep flux measurements (as available in March, 2011) with the solar luminosity constraint, to fix the principal pp-chain fluxes. That is, the sum of the rates for the ppI, ppII, and ppIII cycles, weighted by the energy each cycle deposits in the Sun, is fixed by the photon luminosity. Consequently the “solar values” are not strictly measured ones, but derived assuming a steady-state Sun.

Table 2 also gives fluxes for two solar models, reflecting the metallicity uncertainties mentioned previously. The first model uses abundances for volatile elements that were obtained from an absorption line analysis in which the photosphere was treated in 1D, yielding $(Z/X)_S = 0.0229$ (Grevesse & Sauval 1998). As Solar Fusion II cross sections are used as well, this model is denoted GS98-SFII. The second, denoted AGSS09-SFII, takes abundances from a 3D photospheric model, yielding $(Z/X)_S = 0.0178$ (Asplund et al. 2009). The solar core is sensitive to metallicity, as free-bound/bound-free transitions in metals are an important contributor to the opacity. A low-metallicity Sun, as in model AGSS09-SFII, produces a somewhat cooler core (by $\sim 1\%$), and thus lower fluxes of temperature-sensitive neutrinos, such as those from ^8B β decay.

The SSM fluxes for the CN I cycle β decays of ^{13}N and ^{15}O and the CNO II cycle decay of ^{17}F are also shown. Despite the minor role the CN cycle plays in solar energy generation, these fluxes are significant. The excess in the flux of ^{13}N neutrinos relative to ^{15}O neutrinos in Table 2 is a consequence of the out-of-equilibrium burning of the CN cycle discussed previously.

The SSM uncertainties given in Table 1 are generated from the uncertainties assigned to approximately 20 model input parameters, denoted β_j . These include the solar age, present-day luminosity, opacities, the diffusion constant, the S-factors for the pp chain and CN cycle, and the various metal abundances (key

elements such as C, N, O, Ne, Mg, Si, S, Ar, and Fe). The consequences of input SSM uncertainties on observables are typically parameterized through logarithmic partial derivatives $\alpha(i, j)$, determined by calculating the SSM response to variations in the β_j . For example, in the case of the neutrino fluxes ϕ_i , the

$$\alpha(i, j) \equiv \frac{\partial \ln [\phi_i / \phi_i(0)]}{\partial \ln [\beta_j / \beta_j(0)]} \quad (3)$$

can be found in the SSM updates of Peña-Garay & Serenelli (2008) and Serenelli (2010). Here $\phi_i(0)$ and $\beta_j(0)$ denote the SSM best values.

The partial derivatives define the power-law dependencies of neutrino fluxes with respect to the SSM best-value prediction $\phi_i(0)$,

$$\phi_i \sim \phi_i(0) \prod_{j=1}^{19} \left[\frac{\beta_j}{\beta_j(0)} \right]^{\alpha(i, j)} = \phi_i(0) \prod_{j=1}^{19} [1 + \delta\beta_j]^{\alpha(i, j)}, \quad (4)$$

where $\delta\beta_j \equiv \Delta\beta_j / \beta_j(0)$ is the fractional uncertainty of input parameter β_j with respect to its SSM best value. As this expression separates the impact of SSM parameter variations on ϕ_i into a solar piece – the infinitesimal SSM response described by $\alpha(i, j)$ – and a laboratory or theory piece – the estimated uncertainty $\delta\beta_j$ of an input parameter, the effects of parameter variations can be explored without repeating SSM calculations.

The solar abundance problem is characterized by large systematic differences in the SSM β_j for key abundances. Consequently the differences in the GS98-SFII and AGSS09-SFII SSM neutrino flux predictions of Table 2 exceed their respective internal statistical uncertainties, in several cases. The Table summarizes key helioseismic predictions of both models, with the low-Z AGSS09-SFII SSM predictions being in significantly poorer agreement with the data.

The spectra of solar neutrinos emitted by the Sun is shown in Fig. 3. This familiar figure is somewhat idealized: it includes competing β decay and EC

branches for the p+p reaction, but omits the EC lines that accompany the other β decay reactions of Table 2. The EC branching ratio increases with increasing Z and decreasing Q-value. Thus, among the omitted cases, EC is most significant for the CNO cycle reactions, where rate estimates were made by Stonehill, Formaggio & Robertson (2004). The EC lines shown in the figure are in fact thermally broadened, as they occur in a plasma. Finally, at energies $\lesssim 10$ keV below the scale of Fig. 3, there is a contribution from neutrino pairs of all flavors produced thermally in the solar core (Haxton & Lin 2000): while the flux of these neutrinos is modest, the peak flux density of $\sim 10^9/\text{cm}^2/\text{s}/\text{MeV}$ exceeds that of all solar β decay sources, except for the pp neutrinos.

In the following sections, measurements of the various sources can provide unique information on the structure and composition of the Sun, and on the properties of neutrinos, including how those properties depend on the surrounding environment.

3 EXPERIMENTS: NEUTRINOS AND HELIOSEISMOLOGY

The SSM is a model of the Sun’s interior structure, rather than the more complicated behavior of the convective envelope. The two main tools by which we can probe the solar interior and thus test the validity of the SSM are neutrino spectroscopy and helioseismology. Neutrino fluxes are sensitive to core temperature – a property that responds to changes in the opacity and composition – and to nuclear cross sections. Helioseismic maps of the sound speed throughout much of the solar interior have achieved accuracy of a few parts in 1000, constraining the solar density and pressure profiles, and determining rather precisely the boundary between the Sun’s radiative core and convective envelope.

3.1 Neutrino Spectroscopy: Early Experiments

3.1.1 THE CHLORINE EXPERIMENT Radiochemical detection of neutrinos by $^{37}\text{Cl}(\nu_e, e^-)^{37}\text{Ar}$ was suggested by Pontecorvo (1946) and explored in more detail by Alvarez (1949), who was interested in the possibility of a reactor neutrino experiment to detect a Majorana neutrino. Ray Davis's efforts to develop a practical detector began with his Brookhaven experiment (Davis Jr. 1955), which used a 1000-gallon tank of perchloroethylene (C_2Cl_4) placed 19 feet underground. This yielded an upper bound on the rate for solar neutrino reactions of $\sim 40,000$ SNU. Subsequent developments are described by Lande (2010). Construction began on the Homestake detector in 1965, with first results announced in 1968, and with measurements continuing until 2002, when the Homestake Mine closed. The final result

$$\langle\sigma\phi\rangle = 2.56 \pm 0.16 \pm 0.16 \text{ SNU} \quad (5)$$

is about a factor of three below historical SSM best values. (The SSM GS98-SFII rate is 8.00 ± 0.97 SNU.)

The experiment exploited fortuitous properties of ^{37}Ar in achieving nearly single-atom counting. The average solar neutrino reaction rate in the tank was 0.48 counts/day, above a background dominated by cosmogenics of 0.09 counts/day. As a noble gas that does not interact chemically, argon can be extracted with high efficiency ($\gtrsim 95\%$) from large volumes of organic liquid. The ^{37}Ar half life of ~ 35 days allowed tank concentrations to build up over a saturation time of \sim two months, yet also made ^{37}Ar counting via electron capture feasible. As the decay populates the ground state of ^{37}Cl , the signal is the 2.82 keV Auger electron produced as the electrons in ^{37}Cl adjust to fill the K-shell vacancy. Davis developed miniaturized gas proportional counters for this counting.

Taking into account detector efficiencies and losses due to ^{37}Ar decaying in the tank, the number of Ar atoms counted per year was ~ 25 .

The chlorine experiment was primarily sensitive to the temperature-dependent neutrino fluxes produced in the ppIII and ppII cycles ($^8\text{B} \sim 75\%$, $^7\text{Be} \sim 16\%$). For this reason the source of the “solar neutrino problem” was not immediately apparent. Many candidate explanations were offered over the next 30 years, with many of these proposing changes in the SSM to produce a somewhat cooler core.

3.1.2 KAMIOKANDE II/III Confirmation of the ^{37}Cl results came 21 years later, from a detector originally designed for proton-decay studies. The Kamiokande I proton decay detector was upgraded in the early 1980s to Kamiokande II/III, a 3.0-kiloton imaging water Cherenkov detector capable of detecting solar and other low-energy neutrinos. The neutrino signal is the Cherenkov light emitted by recoiling electrons after elastic scattering (ES), $\nu_x + e^- \rightarrow \nu'_x + e^-$, which is sensitive to both electron and heavy-flavor neutrinos, though with the differential sensitivity $\sigma(\nu_e)/\sigma(\nu_\mu) \sim 6$. For incident neutrino energies $\gg m_e c^2$, the electron is scattered in the forward direction. Thus, by correlating event directions with the position of the Sun, one can cut away a large background uncorrelated with solar position, to reveal solar neutrino events in a forward cone.

The inner 2.14 kilotons of the detector was viewed by 948 20-inch Hamamatsu photomultiplier (PMT) detectors, providing $\sim 20\%$ coverage. The innermost 0.68 kilotons of the detector served as the fiducial volume for solar neutrino detection. Kamiokande II operated with a ~ 9 MeV threshold, which was later reduced to 7.5 and 7.0 MeV in Kamiokande III.

The improvements made in Kamiokande II to enable solar neutrino detection included water purification to reduce low-energy backgrounds associated with

radon and uranium as well as electronics upgrades to improve timing, vital for the reconstruction of the interaction vertices and directions of low-energy electrons, and thus in more cleanly defining a fiducial volume for solar neutrino events. After water-sealing the cavity holding the main detector, the outer portion of the detector was instrumented with 123 PMTs to serve as a muon anti-counter, and additional water was added to shield against γ s from the surrounding rock. Kamiokande III included improvements in the electronics, water purification system, event reconstruction and selection tools, and Monte Carlo detector simulations software.

The first production run of Kamiokande II began in January 1987. The detection of ^8B solar neutrinos based on 450 days of data extending through May 1988 was announced by Kamiokande Collaboration, K. S. Hirata et al. (1989). The measured flux of ^8B neutrinos with energies above 9.3 MeV was found to be $0.46 \pm 0.13(\text{stat}) \pm 0.08(\text{syst})$ of the SSM value, confirming the deficit seen by Davis and collaborators. Kamioka II/III ran until February 1995, collecting 2079 days of data. The combined analysis of all data sets yielded (Kamiokande Collaboration, Y. Fukuda et al. 1996)

$$\phi(^8\text{B}) = (2.80 \pm 0.19(\text{stat}) \pm 0.33(\text{sys})) \times 10^6/\text{cm}^2\text{s}, \quad (6)$$

or 50% (61%) of the GS98-SFII (AGSS09-SFII) SSM result.

The Kamiokande II/III detector was the first to record solar neutrinos event by event, establish their solar origin through correlation with the direction to the Sun, and provide direct information on the ^8B spectrum through the recoil electron spectrum from ES.

3.1.3 THE GALLIUM EXPERIMENTS Two radiochemical gallium experiments exploiting the reaction $^71\text{Ga}(\nu_e, e^-)^71\text{Ge}$, SAGE and GALLEX/GNO, began so-

lar neutrino measurements in January 1990 and May 1991, respectively. SAGE, which continues to operate, uses a target of 50 tons of Ga metal, heated to 30°C so that the metal remains molten, and has reported results for 168 extractions through December 2007. The experiment is located in the Baksan Neutrino Observatory, under Mt. Andyrchi in the Caucasus. GALLEX, which used 30 tons of Ga in the form of a GaCl₃ solution, operated through 1997, and its successor GNO continued through 2003. GALLEX and GNO were mounted in the Gran Sasso National Laboratory, near L'Aquila, Italy.

Gallium, first proposed as a solar neutrino detector by Kuzmin (1966), has a low threshold for solar neutrino absorption (233 keV) and a strong Gamow-Teller transition to the ground state of ⁷¹Ge. This leads to a large cross section for absorbing the low-energy pp neutrinos. As ⁷¹Ge has a half life of 11.43 days, a radiochemical experiment analogous to that done for chlorine was proposed, though the chemistry of Ge recovery is considerably more complicated than that for Ar. Because of its pp neutrino sensitivity, the Ga experiment has a minimum astronomical counting rate of 79 SNU, assuming only a steady-state Sun and standard-model (SM) weak interaction physics. That is, any combination of ppI, ppII, and ppIII burning consistent with the Sun's observed luminosity will lead to a solar neutrino capture rate at or above this value (Bahcall 1989). Thus the gallium experiment had the potential to yield a result that would require a "new physics" solution to the solar neutrino problem.

In 1974 Davis and collaborators began work on the chemistry of Ge recovery for both GaCl₃ solution and Ga metal, conducting a 1.3-ton pilot experiment using GaCl₃ in 1980-82 to demonstrate the procedures later used by GALLEX. The method recovers Ge as GeCl₄ by bubbling nitrogen through the solution, then

scrubbing the gas. The Ge can be further concentrated and purified, converted into GeH_4 , then counted in miniaturized gas proportional counters similar to those used in the chlorine experiment.

In the SAGE experiment with room-temperature liquid metal, the ^{71}Ge is separated by mixing into the gallium a solution of hydrogen peroxide and dilute hydrochloric acid, which produces an emulsion, with the germanium migrating to the surface of the emulsion as droplets, where it can be oxidized and dissolved by hydrochloric acid. The Ge is extracted as GeCl_4 , purified and concentrated, synthesized into GeH_4 , then counted as in the GALLEX experiment. In both GALLEX and SAGE, the overall efficiency of the chemical procedures can be determined by introducing Ge carrier.

A unique aspect of the gallium experiments was the neutrino source experiments done to check overall experimental procedures – chemical extraction, counting, and analysis techniques. The calibrations also checked the capture cross section, as two excited-state transitions not constrained by the ^{71}Ge lifetime contribute to ^7Be neutrino capture. Two GALLEX calibrations and the first SAGE calibration were done with ^{51}Cr sources, while the second SAGE calibration used an ^{37}Ar source. Source intensities were ~ 0.5 MCi. The weighted average (SAGE Collaboration, J. N. Abdurashitov et al. 2009) for the four calibrations, expressed as the ratio R of measured ^{71}Ge to that expected due to the source strength, is $R = 0.87 \pm 0.05$ (1σ). The discrepancy, which exceeds two standard deviations, has attracted some attention due to other short-baseline neutrino anomalies (Abazajian et al. 2012, Gavrin et al. 2011).

SAGE began taking data in December 1989. The capture rate limit obtained from five extractions with 30 tons of gallium, $\lesssim 79$ SNU (90% c.l.) (SAGE Col-

laboration, A. I. Abazov et al. 1991), coincided with the minimum astronomical value. The most recent SAGE combined analysis for all 168 extractions yielded (SAGE Collaboration, J. N. Abdurashitov et al. 2009)

$$\langle\sigma\phi\rangle_{SAGE} = 65.4_{-3.0}^{+3.1}(\text{stat})_{-2.8}^{+2.6}(\text{syst}) \text{ SNU}, \quad (7)$$

or approximately half the un-oscillated SSM best value. GALLEX began taking data in May 1991 and announced first results a year later, a counting rate based on 14 extractions of 83 ± 19 (stat) ± 8 (syst) SNU (GALLEX Collaboration, P. Anselmann et al. 1992). GALLEX completed four campaigns, I through IV, running until 1997. From 65 extractions and 1594 days of data, and including updates due to new pulse-shape analysis methods, GALLEX found (GALLEX Collaboration, W. Hampel et al. 1999; Kaether et al. 2010)

$$\langle\sigma\phi\rangle_{GALLEX \text{ I-IV}} = 73.1_{-6.0}^{+6.1}(\text{stat})_{-4.1}^{+3.7}(\text{syst}) \text{ SNU}. \quad (8)$$

A number of improvements in Ge extraction procedures, electronics, counter efficiency calibrations, and radon event characterization were incorporated into the follow-up experiment GNO. The experiment accumulated 1687 days of running between May 1998 and April 2003. The counting rate from the 58 extractions is

$$\langle\sigma\phi\rangle_{GNO} = 62.9_{-5.3}^{+5.5}(\text{stat})_{-2.5}^{+2.5}(\text{syst}) \text{ SNU}. \quad (9)$$

The weighted average of SAGE, GALLEX, and GNO results is

$$\langle\sigma\phi\rangle_{SAGE+GALLEX+GNO} = 66.1 \pm 3.1 \text{ SNU}, \quad (10)$$

with all uncertainties combined in quadrature (SAGE Collaboration, J. N. Abdurashitov et al. 2009). The SSM GS98-SFII rate is 126.6 ± 4.2 SNU.

3.1.4 HINTS OF NEW PHYSICS In Fig. 4 results of the early experiments are compared to the predictions of the contemporary GS98-SFII SSM. Not only are

the results in disagreement with the SSM, but the pattern of discrepancies is not easily reproduced even if one entertains the possibility of substantial variations in that model. By the early 1990s several analyses (Hata & Langacker 1994; Parke 1995; White, Krauss & Gates 1993) had pointed to apparent contradictions in the pattern of fluxes with respect to SSM predictions,

$$\phi(\text{pp}) \sim 0.9\phi^{\text{SSM}}(\text{pp}) \quad \phi(^7\text{Be}) \sim 0 \quad \phi(^8\text{B}) \sim 0.4\phi^{\text{SSM}}(^8\text{B}). \quad (11)$$

Now variations in the SSM affect the neutrino fluxes principally through their impact on the core temperature T_C . As

$$\frac{\phi(^8\text{B})}{\phi(\text{pp})} \sim T_C^{22}, \quad (12)$$

the observation that $\phi(^8\text{B})/\phi(\text{pp}) \sim 0.4\phi^{\text{SSM}}(^8\text{B})/\phi^{\text{SSM}}(\text{pp})$ would seem to require a cooler solar core, $T_C \sim 0.95 T_C^{\text{SSM}}$. On the other hand, as

$$\frac{\phi(^7\text{Be})}{\phi(^8\text{B})} \sim T_C^{-12}, \quad (13)$$

the observation that $\phi(^7\text{Be})/\phi(^8\text{B}) \ll \phi^{\text{SSM}}(^7\text{Be})/\phi^{\text{SSM}}(^8\text{B})$ would seem to require a hotter core, $T_C > T_C^{\text{SSM}}$, a contradiction. Model-independent analyses assuming undistorted neutrino spectra and a steady-state Sun (so that neutrino fluxes are constrained by the Sun's luminosity) were done by Hata, Bludman & Langacker (1994) and Heeger & Robertson (1996). Their calculations showed that the probability of solutions without new particle physics were in a range of $\sim 2\text{-}3\%$. Heeger & Robertson (1996) further argued that if the luminosity constraint were relaxed, this probability would still be limited to $\sim 4\%$. The likelihood of a new-physics solution to the solar neutrino problem was high.

The conclusion – that the solar neutrino problem might have its origin outside of astrophysics – was additionally supported by a growing body of evidence from helioseismology that validated SSM descriptions of the Sun's interior structure.

3.2 Helioseismology

Measurements and analysis of Doppler shifts of photospheric absorption lines show that the Sun's surface oscillates with amplitudes $\sim 30\text{m}$ and velocities $\sim 0.1\text{ m/s}$, reflecting a variety of interior modes (Gizon & Birch 2005). Turbulence within the Sun's convective zone acts as a random driver of sound waves propagating through the gas. Specific frequencies are enhanced as standing waves, normal eigenmodes that reflect details of solar structure. Here we summarize the basics of solar oscillations, referring readers to Chaplin & Miglio (2013) for a more detailed discussion.

The SSM is characterized by quasi-static pressure $p(r)$, density $\rho(r)$, temperature $T(r)$, entropy $s(r)$, gravitational potential $\phi(r)$, and nuclear energy generation $\epsilon(r)$ profiles that are functions of the radial coordinate r . One can perturb the SSM by introducing small displacements $\delta\vec{r}$ and associated velocities $v(\vec{r}) = \partial\delta\vec{r}/\partial t$, then seek small-amplitude normal-mode solutions (Christensen-Dalsgaard 2002)

$$\rho(\vec{r}, t) \equiv \rho_0(r) + \rho'(\vec{r}, t) \quad \rho'(\vec{r}, t) \sim \rho'(r) Y_{lm}(\theta, \phi) e^{i\omega t} \quad (14)$$

that might account for observed solar surface oscillations.

Solar oscillations can be treated in the adiabatic approximation because the timescale for heat exchange is much longer than the oscillation periods of interest. From the adiabatic index Γ_1 describing the power-law dependence of the pressure on the density and the associated sound speed $c(r)$,

$$\Gamma_1 \equiv \left(\frac{\partial \log p(r)}{\partial \log \rho(r)} \right)_s \quad p(r) = \frac{1}{\Gamma_1} \rho(r) c^2(r), \quad (15)$$

one can define an auxiliary field $\Psi(\vec{r}) = c^2 \sqrt{\rho(r)} \vec{\nabla} \cdot \delta\vec{r}$. In the Cowling (neglecting perturbations to the gravitational field) and adiabatic approximations (Duebner

& Gough 1984)

$$\frac{d^2\Psi_l(r)}{dr^2} + \frac{1}{c^2} \left[\omega^2 - \omega_{co}^2 - \frac{l(l+1)c^2}{r^2} \left(1 - \frac{N^2}{\omega^2} \right) \right] \Psi_l(r) \equiv \left(\frac{d^2}{dr^2} + \frac{\omega_{eff}^2}{c^2} \right) \Psi_l(r) \sim 0, \quad (16)$$

where propagating (evanescent) solutions exist for $\omega_{eff}^2 > 0$ (< 0). This eigenvalue problem is governed by the buoyancy, or Brunt-Väisälä, frequency $N(r)$,

$$N^2(r) = \frac{Gm(r)}{r} \left(\frac{1}{\Gamma_1} \frac{d \log p(r)}{dr} - \frac{d \log \rho(r)}{dr} \right), \quad (17)$$

which turns negative in the convective zone but is positive and roughly constant in the radiative interior; the Lamb frequency,

$$S_l^2(r) = \frac{l(l+1)c^2}{r^2}, \quad (18)$$

which diverges for $r \rightarrow 0$ if $l > 0$; and the acoustic cutoff frequency, which depends on the density scale height $H(r)$ and sound speed,

$$\omega_{co}(r) = \frac{c}{2H} \sqrt{1 - 2 \frac{dH}{dr}} \quad \text{where} \quad H(r) \equiv - \left(\frac{1}{\rho(r)} \frac{d\rho(r)}{dr} \right)^{-1}, \quad (19)$$

and determines the outer turning point where $\omega \sim \omega_{co}$. Eigensolutions of Eq. (16) can be found for discrete frequencies $\{\omega_{nl}\}$, where n is the radial order: there is no dependence on m because all azimuthal modes for fixed n, l are degenerate by spherical symmetry. The assumptions leading to Eq. (16) can be justified except when n and l are small, or when $l \ll n$ (Duebner & Gough 1984).

As $\omega \gg \omega_{co}$ everywhere except near the surface, the solar regions supporting propagating solutions are determined by

$$\omega_{eff}^2 \sim \omega^2 - \frac{l(l+1)c^2}{r^2} \left(1 - \frac{N^2}{\omega^2} \right) > 0. \quad (20)$$

Two different families of solutions exist. The g-mode family is determined by the conditions $\omega^2 \ll N^2$ and $\omega^2 \ll S_l^2$. Consequently g-mode propagation is confined

to the solar radiative interior. The second family, the acoustic oscillations or p-modes, are the modes that have been observed in the Sun. If $\omega^2 \gg N^2$, then Eq. (20) and the requirement $\omega_{\text{eff}}^2 > 0$ define the inner turning-point radius

$$r_{\text{turning}} \sim \frac{c(r)}{\omega} \sqrt{l(l+1)}. \quad (21)$$

Qualitatively it is clear that the dependence of the eigenfrequencies on l can provide localized sensitivity to $c(r)$, with modes of low l penetrating more deeply into the solar interior. Because the eigenfrequencies depend on $c(r)$, the p-mode observations constraint the solar pressure and density profiles.

Similar radial sensitivity is found for the g-modes. The condition $\omega \ll N(r)$ allows propagation in the deep interior, as Eq. (20) guarantees that $\omega_{\text{eff}}^2 > 0$ for r sufficiently small. While in principle this suggests sensitivity to $c(r)$ in the solar core, g-modes are damped in the convective envelope, making observation difficult. No undisputed detection exists to date (Appourchaux et al. 2010).

The significant effort invested in helioseismological measurements and analysis has yielded a rather precise map of $c(r)$ over the outer 90% of the Sun by radius. The solar profile used in Fig. 5 was obtained by Basu et al. (2009) from an analysis that included 4752 days of BiSON data (<http://bison.ph.bham.ac.uk>). The comparison SSMs are AGSS09-SFII ($(Z/X)_S = 0.0178$) and GS98-SFII ($(Z/X)_S = 0.0229$).

GS98-SFII is representative of models that were in use in the 1990s: the generally good agreement with the solar $c(r)$ ($\sim 0.2\%$ apart from a narrow region just below the convective boundary) was taken as strong support for the SSM, helping to reinforce the conclusion that the solar neutrino problem might have a particle physics origin. Helioseismic data forced improvements in the SSM, such as the inclusion of helium and heavy-element diffusion (Bahcall & Pinnsoneault

1995, Bahcall & Pinsonneault 1992). The suggestion from early solar neutrino experiments and helioseismology that new particle physics could be the source of the solar neutrino problem provided additional motivation for a new generation of sophisticated experiments with high statistics and sensitivity to neutrino flavor, spectral distortions, and day-night differences, described below.

3.3 Super-Kamiokande

Super-Kamiokande, the successor to the Kamiokande detector, is a 50-kton cylindrical water Cherenkov detector located in the Kamioka Mine at a depth of ~ 2.03 km of water (flat site equivalent). The inner 32-ktons of water is viewed by $\sim 11,100$ 20" photomultipliers (40% coverage), with 22.5-ktons serving as the fiducial volume for detecting solar neutrinos. The detector has operated at (total) electron energy thresholds for solar neutrinos ranging from 7.0 to the present 4.0 MeV, so that detection is limited to ^8B and hep neutrinos. While in ES the energy of the incident neutrino is shared between the scattered electron and outgoing neutrino, electron detection provides some sensitivity to the initial neutrino spectrum and thus to distortions associated with neutrino oscillations (Super-Kamiokande Collaboration 2012; Super-Kamiokande Collaboration, S. Fukuda et al. 2003). The electron energy resolution at 10 MeV is $\sim 16\%$.

The detector began operations in 1996, progressing from phase I to the current phase IV. Super-Kamiokande I recorded neutrino events for approximately five years, determining an ^8B neutrino flux of $\phi(^8\text{B}) = (2.35 \pm 0.02 \text{ (stat)} \pm 0.08 \text{ (syst)}) \times 10^6/\text{cm}^2/\text{s}$ from events recorded above 5 MeV, assuming an undistorted spectrum (Super-Kamiokande Collaboration, J. Hosaka et al. 2006). The measured rate variation of $\sim 7\%$ over the year is consistent in magnitude and

phase with the effects of the Earth's orbital eccentricity, 1.7%. No evidence was found for spectral distortions or day-night differences, two signatures of neutrino oscillations in matter.

The detector was drained following phase I for repairs and maintenance. During refilling the implosion of a phototube led to a blast wave that destroyed most of the lower part of the detector. Super-Kamiokande II was subsequently rebuilt with the remaining phototubes enclosed in blast shields. Despite the reduced phototube coverage of 19% and resulting higher threshold of 7 MeV, Super-Kamiokande II ran successfully as a solar neutrino detector for three years, beginning in late 2002. The deduced rate, $\phi(^8\text{B}) = (2.38 \pm 0.05 \text{ (stat)} \pm_{-0.15}^{+0.16} \text{ (sys)}) \times 10^6/\text{cm}^2/\text{s}$, is consistent with Super-Kamiokande I results. No spectral distortion was detected, and the day-night difference was again consistent with zero at 1σ (Super-Kamiokande Collaboration, J. P. Cravens et al. 2008).

Super-Kamiokande III (Super-Kamiokande Collaboration, K. Abe et al. 2011) collected nearly two years of data between October 2006 and August 2008, operating with a fully restored set of 11129 PMTs equipped with blast shields, providing 40% phototube coverage. Improvements made to the water purification system, event reconstruction and selection tools, and the Monte Carlo detector simulation software resulted in a reduced systematic uncertainty of $\pm 2.1\%$. The observed event rate for electrons between 5.0 and 20 MeV is equivalent to an unoscillated ^8B neutrino flux of $(2.39 \pm 0.04 \text{ (stat)} \pm 0.05 \text{ (sys)}) \times 10^6/\text{cm}^2/\text{s}$ (Smy 2012). No significant spectral distortion was observed.

Preliminary results from 1069 days of running for Super-Kamiokande IV were reported at Neutrino 2012 (Smy 2012). This latest phase of Super-Kamiokande includes new electronics, an improved Monte Carlo model of the trigger efficiency,

higher efficiency due to relaxed cuts against radioactivity backgrounds, and a lower threshold of 4 MeV (total energy).

3.4 Sudbury Neutrino Observatory

A second remarkable detector, the Sudbury Neutrino Observatory (SNO), was constructed two kilometers below ground, within the INCO Creighton nickel mine, Ontario, Canada (Jelley, McDonald & Robertson 2009). A kiloton of heavy water was contained in a 12m-diameter spherical acrylic vessel. A surrounding array of 9500 20-cm PMTs viewed the inner volume, providing $\sim 56\%$ coverage. Seven kilotons of light water provided a 5m buffer between the central detector and the surrounding rock walls.

SNO was proposed by Chen (1985), who recognized the advantages of the multiple detection channels that could be introduced by replacing the hydrogen in an ordinary water Cherenkov detector with deuterium. The flux of higher energy solar electron neutrinos can be probed with the charged-current (CC) reaction

$$\nu_e + d \rightarrow p + p + e^-, \quad (22)$$

with detection of the produced electron. As the Gamow-Teller strength is concentrated near the 1.44 MeV breakup threshold for deuterium, the electrons carry off most of the energy, and thus provide significant information on the incident neutrino spectrum. A second channel, the neutral-current (NC) reaction

$$\nu_x + d \rightarrow \nu'_x + n + p, \quad (23)$$

is independent of the neutrino flavor x , counting all neutrinos above the 2.22 MeV breakup threshold. As the only detectable signal of the reaction is the produced neutron, this channel placed very stringent constraints on the radioactive

cleanliness of the detector. The third channel is the ES reaction of conventional water detectors,

$$\nu_x + e^- \rightarrow \nu'_x + e^{-'}. \quad (24)$$

Operations were carried out in three phases. SNO I operated with pure heavy water. The NC-channel neutrons can capture on deuterium, producing 6.25-MeV gamma rays that Compton scatter off electrons, producing light for recoils above the Cherenkov threshold. SNO I operations covered 306.4 live days from November 1999 through May 2001. Two analyses were performed based on the assumption of an undistorted ^8B spectrum, using electron kinetic energy thresholds of 6.75 and 5 MeV, respectively. The second analysis thus included NC events.

In SNO II two tons of purified NaCl were dissolved in the water, so that $^{35}\text{Cl}(n,\gamma)$ would become the dominant neutron sink. This reaction increases the capture rate and energy release. Data were accumulated for 391.4 live days from July 2001 through August 2003. Detector calibrations completed in SNO I were repeated and extended in SNO II, including new checks involving the introduction of beta-gamma sources that could lead to photo-disintegration of deuterium and the use of a ^{252}Cf neutron source to determine the neutron detection efficiency. The analysis was performed for a kinetic energy threshold of 5.5 MeV and treated the first 254.2 live days of data as blind. In addition, the ^8B spectrum shape was not assumed, but rather extracted from the analysis, using 0.5 MeV bins from 5.5 to 13.5 MeV, plus an additional bin for events between 13.5 and 20 MeV.

In the first two phases of SNO the CC, ES, and NC rates were determined by a statistical analysis that decomposed the common signal, the Cherenkov light, into the three contributing components. The analysis exploited distinguishing angular

correlations with respect to the Sun and energy differences in the CC-, ES-, and NC-associated light. In SNO III the separation of the NC and CC/ES signals was done by direct counting of NC neutrons. The salt introduced in SNO II was removed by reverse osmosis and ion exchange, and a month of data was taken to confirm that the detector had been restored to the operating conditions of SNO I. Then an array of the specially designed ^3He - and CF_4 -filled gas proportional counters was installed for neutron detection by $^3\text{He}(n,p)^3\text{H}$. This neutral-current detection (NCD) array consisted of 40 strings of proportional counters, ranging in length from 9 to 11 meters, that were anchored to the inner surface of the acrylic vessel, forming a lattice on a one-meter grid.

Between November 2004 and November 2006 385.17 live days of SNO III data were taken. Extensive calibrations of both the NCD and PMT arrays were made, utilizing various neutron and gamma-ray sources, in order to calibrate the effectiveness of the neutron detection and the impact of array installation on detector behavior. The array was exploited to characterize neutron backgrounds within the detector, including the distribution and isotopic composition of background sources. During solar neutrino running, data were culled to eliminate strings that exhibited mechanical or electrical faults, or runs (operational periods of at least 30 minutes) when any array abnormalities were observed. A blind analysis of the remaining data was then performed. The neutrino spectrum was again determined from the CC and ES data, not assumed.

The SNO I/II and SNO III results are in generally good agreement, and both separately and in combination established

1. A total flux of active neutrinos from ^8B decay of $\phi_{\text{NC}}(\nu_{\text{active}}) = (5.25 \pm 0.16(\text{stat})_{-0.13}^{+0.11}(\text{syst})) \times 10^6/\text{cm}^2/\text{s}$, in good agreement with SSM predictions,

and $\phi_{\text{CC}}(\nu_e) \sim 0.34 \phi_{\text{NC}}(\nu_{\text{active}})$; and

2. The absence of statistically significant day-night effects or spectral distortions in the portion of the ^8B neutrino spectrum above ~ 5 MeV;

3.5 Borexino

The Borexino experiment (Borexino Collaboration, G. Alimonti et al. 2009), located in the Gran Sasso Laboratory at an effective depth of about 3.0 km.w.e., is the first to measure low-energy (< 1 MeV) solar neutrino events in real time. The detector is housed within a 16.9m domed tank containing an outer layer of ultrapure water that provides shielding against external neutrons and gamma rays. At the inner edge of the water a stainless steel sphere serves as a support structure for an array of photomultiplier tubes that view both the inner detector and the outer water shield, so that the Cherenkov light emitted by muons passing through the water can be used to veto those events. Within the steel sphere there are two regions, separated by thin nylon vessels, containing high-purity buffer liquid, within which is sequestered a central volume of 278 tons of organic scintillator. The fiducial volume consists of ~ 100 tons of the liquid scintillator at the very center of the detector. Scintillation light produced by recoil electrons after ES events is the solar neutrino signal. The 862 keV ^7Be neutrinos produce a recoil electron spectrum with a distinctive cut-off edge at 665 keV.

The Borexino Collaboration reported results in 2008 and 2011 constraining the fluxes of three low-energy solar neutrino branches (Borexino Collaboration, G. Bellini et al. 2011, 2012a):

1. A ^7Be solar rate equivalent to an unoscillated flux of $(3.10 \pm 0.15) \times 10^9 / \text{cm}^2\text{s}$, or about 62% of the GS98-SFII SSM central value;

2. A ES rate for ${}^8\text{B}$ neutrinos, based on a integration above 3 MeV, corresponding to an equivalent flux of $\phi^{\text{ES}}({}^8\text{B}) = (2.4 \pm 0.4 \pm 0.1) \times 10^6/\text{cm}^2\text{s}$ (Borexino Collaboration, G. Bellini et al. 2010), less precise than but in good agreement with SNO and Super-Kamiokande results. [A similar result has been obtained by the KamLAND collaboration, $\phi^{\text{ES}}({}^8\text{B}) = (2.77 \pm 0.26 \pm 0.32) \times 10^6/\text{cm}^2\text{s}$ from events above their 5.5 MeV analysis threshold (KamLAND Collaboration, S. Abe et al. 2011).]
3. The first direct, exclusive determination of the pep flux, $(1.6 \pm 0.3) \times 10^8/\text{cm}^2\text{s}$ (95% c.l.); and
4. A limit on the CNO neutrino flux, $\phi_{\text{CNO}} < 7.7 \times 10^8/\text{cm}^2\text{s}$ at 95% c.l.

The Borexino ${}^7\text{Be}$ measurement places an important constraint on matter effects in neutrino oscillations, as this line lies in a region dominated by vacuum oscillations, while the Super-Kamiokande and SNO measurements are done in the matter-dominated region.

4 NEW NEUTRINO PROPERTIES

The results just described have been addressed in global analyses that extract from the experiments constraints on neutrino and solar properties. Before describing such analyses, we discuss some of the associated weak interactions issues. As previously noted, by 1994 Kamiokande II/III had finished operations, confirming the neutrino deficit that Davis, Harmer, and Hoffman had first discovered 26 years earlier, and the SAGE and GALLEX experiments had converged on a counting rate very close to the minimum astronomical value of 78 SNU. The pattern of pp, ${}^7\text{Be}$, and ${}^8\text{B}$ fluxes that emerged from analyses of the three early experiments (see Eq. (11)) was inconsistent with possible SSM variations altering

T_C (see figures by Castellani et al. (1994) and Hata, Bludman & Langacker (1994) included in Haxton (1995)) and improbable in model-independent analyses that assumed only undistorted neutrino spectra (Hata, Bludman & Langacker 1994; Heeger & Robertson 1996). The agreement between the SSM sound speed profile and that deduced from helioseismology also made it more difficult to motivate SSM changes.

A variety of new particle physics solutions to the solar neutrino problem had been suggested over the years, including vacuum and matter-enhanced neutrino oscillations, neutrino decay (Bahcall, Cabibbo & Yahil 1972), and weakly interacting massive particles (WIMPs) that might be bound in the Sun and consequently contribute to energy transport (Faulkner & Gilliland 1985, Spergel & Press 1985). In addition to the standard MSW scenario, other oscillation effects in matter were explored, including spin-flavor resonances driven by neutrino magnetic moments (Akhmedov 1988, Lim & Marciano 1988), parametric density fluctuations (Krastev & Smirnov 1989, Schafer & Koonin 1987), contributions to the MSW potential from currents (Haxton & Zhang 1991), and depolarization in the stochastic fluctuation limit (Loreti & Balantekin 1994).

Of these and other possibilities, the MSW mechanism drew the most attention because of its minimal requirements, neutrino masses and a vacuum mixing angle $\theta_v \gtrsim 10^{-4}$. While neutrinos are massless in the SM, and consequently cannot oscillate, nonzero masses arise in most extensions of the model. Small weak interaction mixing angles were already familiar from the analogous quark mixing matrix.

4.1 Oscillation Basics: The Vacuum Case

The current laboratory (tritium β decay) limit on the $\bar{\nu}_e$ mass is 2.3 eV, though an effort is underway to substantially improve this bound (KATRIN Collaboration, J. Angrik et al. 2004; Otten & Weinheimer 2008). Cosmological analyses variously limit the sum over mass eigenstates to $\sum_i m_\nu(i) \lesssim 0.2 - 0.6$ eV (Abazajian et al. 2011).

Two types of neutrino mass terms can be added to the SM. Neutrinos can have Dirac masses, analogous to those of other SM fermions, if the SM is enlarged to include a right-handed neutrino field. Because neutrinos lack charges or other additively conserved quantum numbers, lepton-number-violating Majorana mass terms can also be added, $\overline{\nu}_L^c m_L \nu_L$ and $\overline{\nu}_R^c m_R \nu_R$, where the former is the only dimension-five operator that can be constructed in the SM. (The subscripts L and R denote left- and right-hand projections of the neutrino field ν , and the superscript c denotes charge conjugation.)

In the seesaw mechanism (Gell-Mann, Ramond & Slansky 1979; Mohapatra & Senjanovic 1980; Yanagida 1980) the Dirac and Majorana mass terms are combined in a manner that provides an attractive explanation for light neutrinos,

$$M_\nu \sim \begin{pmatrix} 0 & m_D \\ m_D^T & m_R \end{pmatrix},$$

where $m_L \sim 0$ in part because of double beta decay constraints. When diagonalized, the matrix yields heavy and light neutrino mass eigenstates,

$$m_H \sim m_R \qquad m_L \sim m_D \frac{m_D}{m_R}$$

with the latter related to the typical Dirac mass of the SM by the coefficient m_D/m_R . If we assume the scale of the new physics which m_R represents is

$\gg m_D$, then a candidate small parameter m_D/m_R is available to explain why neutrinos are so much lighter than other SM fermions. Small neutrino masses are thus explained as a consequence of the scale m_R of new physics beyond the SM.

Neutrinos of definite mass are the stationary states for free propagation, while neutrino flavor eigenstates are produced in weak interactions. Simplifying here to two flavors, the relationship of the flavor $\{\nu_e, \nu_\mu\}$ and mass $\{\nu_1, \nu_2\}$ eigenstates can be described by a single vacuum mixing angle θ_v ,

$$\nu_e = \cos \theta_v |\nu_1\rangle + \sin \theta_v |\nu_2\rangle \quad \nu_\mu = -\sin \theta_v |\nu_1\rangle + \cos \theta_v |\nu_2\rangle. \quad (25)$$

Consequently, an arbitrary initial state $|\nu(t=0)\rangle = a_e(t=0)|\nu_e\rangle + a_\mu(t=0)|\nu_\mu\rangle$ of momentum $k \sim E$, as it propagates downstream, evolves according to

$$i \frac{d}{dt} \begin{pmatrix} a_e \\ a_\mu \end{pmatrix} = \frac{1}{4E} \begin{pmatrix} -\delta m_{21}^2 \cos 2\theta_v & \delta m_{21}^2 \sin 2\theta_v \\ \delta m_{21}^2 \sin 2\theta_v & \delta m_{21}^2 \cos 2\theta_v \end{pmatrix} \begin{pmatrix} a_e \\ a_\mu \end{pmatrix}. \quad (26)$$

where an average overall wave function phase has been removed from the neutrino mass matrix (represented in the flavor basis). For the special case of a ν_e produced at time $t = 0$, the solution of this equation yields

$$P_{\nu_e}(t) = |\langle \nu_e | \nu(t) \rangle|^2 = 1 - \sin^2 2\theta_v \sin^2 \left(\frac{\delta m_{21}^2 t}{4E} \right) \rightarrow 1 - \frac{1}{2} \sin^2 2\theta_v \quad (27)$$

where the downstream oscillation depends on the difference $\delta m_{21}^2 \equiv m_2^2 - m_1^2$. (If this problem is done properly with wave packets, the oscillation persists until the two mass components separate spatially, yielding the asymptotic result on the right.) The oscillation length $L_0 = 4\pi\hbar c E / \delta m_{21}^2 c^4$ is shorter than the Earth-Sun distance for a typical solar neutrino of energy ~ 1 MeV provided $\delta m_{21}^2 \gtrsim 1.6 \times 10^{-11} \text{ eV}^2$. Thus solar neutrinos are interesting for oscillation studies because of their sensitivity to extremely small neutrino mass differences.

4.2 Oscillation Basics: Matter and the MSW Mechanism

Mikheyev & Smirnov (1985, 1986) showed that the density dependence of the neutrino effective mass, a phenomenon first discussed by Wolfenstein (1978a,b), could greatly enhance oscillation probabilities. Their original numerical work was soon understood analytically as a consequence of level crossing: a neutrino produced in the core as a ν_e is adiabatically transformed into a ν_μ by traversing a critical solar density where the ν_e and ν_μ effective masses cross. It became clear that the Sun is not only an excellent neutrino source, but also a natural regenerator for enhancing the effects of flavor mixing.

Equation (26) describing vacuum oscillations is altered in matter

$$i \frac{d}{dx} \begin{pmatrix} a_e \\ a_\mu \end{pmatrix} = \frac{1}{4E} \begin{pmatrix} 2E\sqrt{2}G_F\rho(x) - \delta m_{21}^2 \cos 2\theta_v & \delta m_{21}^2 \sin 2\theta_v \\ \delta m_{21}^2 \sin 2\theta_v & -2E\sqrt{2}G_F\rho(x) + \delta m_{21}^2 \cos 2\theta_v \end{pmatrix} \begin{pmatrix} a_e \\ a_\mu \end{pmatrix} \quad (28)$$

where G_F is the weak coupling constant and $\rho(x)$ the solar electron number density. The new contribution to the difference in diagonal elements, $4E\sqrt{2}G_F\rho(x)$, represents the effective contribution to m_ν^2 that arises from neutrino-electron scattering. The indices of refraction of electron and muon neutrinos differ because the former scatter via charged and neutral currents, while the latter have only neutral current interactions. For $\theta_v \lesssim \pi/4$ – the “normal hierarchy” where the lighter mass eigenstate makes the larger contribution to ν_e in vacuum – the matter and vacuum contributions to the diagonal elements of Eq. (28) have opposite signs.

We can diagonalize the right-hand side of Eq. (28) to determine the heavy and light local mass eigenstates and eigenvalues $m_H(x)$ and $m_L(x)$, functions of $\rho(x)$

$$|\nu_L(x)\rangle = \cos\theta(x)|\nu_e\rangle - \sin\theta(x)|\nu_\mu\rangle \quad |\nu_H(x)\rangle = \sin\theta(x)|\nu_e\rangle + \cos\theta(x)|\nu_\mu\rangle \quad (29)$$

where the local mixing angle

$$\sin 2\theta(x) = \frac{\sin 2\theta_v}{\sqrt{X^2(x) + \sin^2 2\theta_v}} \quad \cos 2\theta(x) = \frac{-X(x)}{\sqrt{X^2(x) + \sin^2 2\theta_v}} \quad (30)$$

depends on $X(x) = 2\sqrt{2}G_F\rho(x)E/\delta m_{21}^2 - \cos 2\theta_v$. Unlike the vacuum case, these are stationary states for propagation only if $\rho(x)$ is constant. Otherwise, defining $|\nu(x)\rangle = a_H(x)|\nu_H(x)\rangle + a_L(x)|\nu_L(x)\rangle$, Eq. (28) becomes

$$i\frac{d}{dx} \begin{pmatrix} a_H \\ a_L \end{pmatrix} = \frac{1}{4E} \begin{pmatrix} \lambda(x) & i\alpha(x) \\ -i\alpha(x) & -\lambda(x) \end{pmatrix} \begin{pmatrix} a_H \\ a_L \end{pmatrix}. \quad (31)$$

The splitting of the local mass eigenstates and the local oscillation length are

$$\lambda(x) = \delta m_{21}^2 \sqrt{X^2(x) + \sin^2 2\theta_v} \quad L_0(x) = \frac{4\pi\hbar c E}{\lambda(x)c^4} \quad (32)$$

while eigenstate mixing is governed by the density gradient

$$\alpha(x) = \left(\frac{4E^2}{\delta m_{21}^2} \right) \frac{\sqrt{2}G_F \frac{d}{dx}\rho(x) \sin 2\theta_v}{X^2(x) + \sin^2 2\theta_v}. \quad (33)$$

The splitting achieves its minimum value, $2\delta m_{21}^2 \sin 2\theta_v$, at a critical density $\rho_c = \rho(x_c)$ where $X(x) \rightarrow 0$,

$$2\sqrt{2}EG_F\rho_c = \delta m_{21}^2 \cos 2\theta_v. \quad (34)$$

The diagonal elements of the original flavor matrix of Eq. (28) cross at ρ_c .

The crux of the MSW mechanism is the adiabatic crossing of the critical density, illustrated in the left panel of Fig. 6. The adiabatic condition is determined by the requirement $\gamma(x) = \left| \frac{\lambda(x)}{\alpha(x)} \right| \gg 1$, which allows one to treat Eq. (31) as diagonal.

This condition becomes particularly stringent near the crossing point,

$$\gamma_c \equiv \gamma(x_c) = \frac{\sin^2 2\theta_v}{\cos 2\theta_v} \frac{\delta m_{21}^2}{2E} \frac{1}{\left| \frac{1}{\rho_c} \frac{d\rho(x)}{dx} \Big|_{x=x_c} \right|} = 2\pi \tan 2\theta_v \frac{H_c}{L_c} \gg 1, \quad (35)$$

where H_c and L_c are the solar density scale height and local oscillation length at x_c . If the $H_c \gg L_c$, Eq. (31) then yields (Bethe 1986)

$$P_{\nu_e}^{\text{adiab}} = \frac{1}{2} + \frac{1}{2} \cos 2\theta_v \cos 2\theta_i \quad (36)$$

where $\theta_i = \theta(x_i)$ is the local mixing angle at the density where the neutrino is produced. The adiabatic solution depends on the local mixing angles where the neutrino begins (θ_i , solar core) and ends (θ_v , in vacuum) its propagation.

For illustration, consider the case of a small $\theta_v \sim 0$. A solar ν_e created in the high-density solar core is then nearly identical to the heavy-mass eigenstate ($\theta_i \sim \pi/2$), provided the vacuum mass difference between the eigenstates is not too large (see Eq. (30)). If the subsequent propagation is adiabatic, the neutrino remains on the heavy-mass trajectory, crossing the critical density ($\theta(x_c) = \pi/4$), and finally exiting the Sun. But in vacuum the heavy mass eigenstate is $\sim \nu_\mu$: a nearly complete flavor change, $\nu_e \rightarrow \nu_\mu$, has occurred, through an adiabatic rotation of the local oscillation angle from $\theta_i \sim \pi/2$ to $\theta_f = \theta_v$ during propagation.

If the adiabatic condition is not satisfied, e.g., $\gamma_c \lesssim 1$, an accurate analytic solution can still be obtained (Haxton 1986, Parke 1986). As we have seen, the nonadiabatic behavior is governed by the density scale height at x_c . One can replace the actual solar density by an effective one, e.g., a linear density “wedge” that has the correct derivative at x_c (thereby incorporating the effects of the density gradient at the most sensitive point), while also starting and ending at the appropriate initial and final densities (thereby also building in the adiabatic limit). The resulting generalization of Eq. (36) is

$$P_{\nu_e} = \frac{1}{2} + \frac{1}{2} \cos 2\theta_v \cos 2\theta_i (1 - 2P_{\text{hop}}) \quad P_{\text{hop}} \equiv e^{-\pi\gamma_c/2} \quad (37)$$

where P_{hop} , the Landau-Zener probability of hopping from the heavy mass trajectory to the light trajectory on traversing x_c , vanishes in the highly adiabatic limit, $\gamma_c \gg 1$ (so that Eq. (37) reduces to Eq. (36)). When the crossing becomes highly nonadiabatic ($\gamma_c \ll 1$), $P_{\text{hop}} \rightarrow 1$: the neutrino exits the Sun on the light mass trajectory, which for small mixing angles means it remains $\sim \nu_e$.

Thus strong conversion of solar neutrinos is expected when 1) the propagation is adiabatic ($\gamma_c \gtrsim 1$) and 2) there is a level crossing (there is enough matter at the ν_e production point that $\nu_e(x_i) \sim \nu_H(x_i)$). The right panel of Fig. 6 shows the white triangle of parameters in the $\delta m_{21}^2/E - \sin^2 2\theta_v$ plane where both constraints are satisfied. Within this triangle, strong conversion occurs. One can envision superimposing on this triangle the spectrum of solar neutrinos, plotted as a function of $\delta m_{21}^2/E$ for some choice of δm_{21}^2 and θ_v . Depending on how that spectrum is positioned vertically (a function of δm_{21}^2) or horizontally (a function of θ_v) one can alter the resulting spectrum of ν_e s in several characteristic ways, for example, suppressing the low-energy or high-energy neutrinos preferentially, or even (in the case of small mixing angles) those of intermediate energy.

In early fits to the neutrino data three potential MSW solutions were frequently discussed, designated by SMA (small mixing angle: $\delta m_{21}^2 \sim 5.4 \times 10^{-6}$ eV, $\sin^2 2\theta \sim 0.006$), LMA (large mixing angle: $\delta m_{21}^2 \sim 1.8 \times 10^{-5}$ eV, $\sin^2 2\theta \sim 0.76$), and LOW (low probability, low mass: $\delta m_{21}^2 \sim 7.9 \times 10^{-8}$ eV, $\sin^2 2\theta \sim 0.96$). (The parameter values are taken from Bahcall, Krastev & Smirnov (1998) and are representative of fits done at that time.) These solutions are indicated schematically by the colored regions in Fig. 6. The solution consistent with the solar neutrino data proved, ironically, to be the LMA solution – not the SMA solution where matter effects so greatly enhance the oscillations.

5 GLOBAL ANALYSES AND NEUTRINO PROPERTIES

Neutrino physics has made great progress in the last 15 years, as reactor and accelerator neutrino experiments have added new information to that obtained from solar and atmospheric neutrino experiments. The three mixing angles of the 3×3

neutrino mass matrix, the magnitudes of the two mass differences, and from solar neutrino experiments the sign of one of these have all been determined. The phenomena that can be explored with solar neutrinos were illustrated previously for the two-flavor case: flavor oscillations, affected by matter, not only alter fluxes, but lead to distinctive spectral distortions, and may produce day-night differences due to neutrino passage through the Earth. The various experimental collaborations as well as independent groups have developed global analysis methods to analyze solar neutrino experiments, taking into account the constraints other recent measurements have imposed. Here we summarize the conclusions of such analyses, relying particularly on work done by the Bari and Valencia groups.

5.1 Vacuum Mixing Angles and Mass² Differences

In the SM case of three light neutrino flavors, the relationship between flavor $\{\nu_e, \nu_\mu, \nu_\tau\}$ and mass $\{\nu_1, \nu_2, \nu_3\}$ eigenstates is described by the PMNS matrix (Maki, Nakagawa & Sakata 1962; Pontecorvo 1967)

$$\begin{pmatrix} |\nu_e\rangle \\ |\nu_\mu\rangle \\ |\nu_\tau\rangle \end{pmatrix} = \begin{pmatrix} c_{12}c_{13} & s_{12}c_{13} & s_{13}e^{-i\delta} \\ -s_{12}c_{23} - c_{12}s_{23}s_{13}e^{i\delta} & c_{12}c_{23} - s_{12}s_{23}s_{13}e^{i\delta} & s_{23}c_{13} \\ s_{12}s_{23} - c_{12}c_{23}s_{13}e^{i\delta} & -c_{12}s_{23} - s_{12}c_{23}s_{13}e^{i\delta} & c_{23}c_{13} \end{pmatrix} \begin{pmatrix} e^{i\alpha_1/2}|\nu_1\rangle \\ e^{i\alpha_2/2}|\nu_2\rangle \\ |\nu_3\rangle \end{pmatrix} \quad (38)$$

where $c_{ij} \equiv \cos \theta_{ij}$ and $s_{ij} \equiv \sin \theta_{ij}$. This matrix depends on three mixing angles θ_{12} , θ_{13} , and θ_{23} , of which the first and last are the dominant angles for solar and atmospheric oscillations, respectively; a Dirac phase δ that can induce CP-violating differences in the oscillation probabilities for conjugate channels such as $\nu_\mu \rightarrow \nu_e$ versus $\bar{\nu}_\mu \rightarrow \bar{\nu}_e$; and two Majorana phases α_1 and α_2 that will affect the interference among mass eigenstates in the effective neutrino mass probed in

the lepton-number-violating process of neutrinoless double β decay.

It became apparent in early analyses that combined solar and reactor neutrino data in two-flavor analyses that there was some hint of the third flavor, a nonzero θ_{13} . The KamLAND Collaboration analysis employed the three-flavor ν_e survival probability of Fogli et al. (2000) in which the influence of θ_{13} in modifying the two-flavor result is explicit,

$$P_{ee}^{3\nu} = \cos^4 \theta_{13} \tilde{P}_{ee}^{2\nu} + \sin^4 \theta_{13} \quad (39)$$

where $\tilde{P}_{ee}^{2\nu}$ is the two-flavor survival probability in matter evaluated for the modified electron density $\rho(x) \rightarrow \rho(x) \cos^2 \theta_{13}$. The analysis yielded $\sin^2 \theta_{13} = 0.020 \pm 0.016$ (KamLAND Collaboration, A. Gando et al. 2011), a result consistent with the long-baseline ν_e appearance results announced shortly afterwards, $0.008 \lesssim \sin^2 \theta_{13} \lesssim 0.094$ (T2K Collaboration, K. Abe et al. 2011) and $0.003 \lesssim \sin^2 \theta_{13} \lesssim 0.038$ (MINOS Collaboration, P. Adamson et al. 2011). In 2012 results from reactor $\bar{\nu}_e$ disappearance experiments became available, yielding $\sin^2 \theta_{13} = 0.022 \pm 0.011(\text{stat}) \pm 0.008(\text{sys})$ (Double Chooz Collaboration, Y. Abe et al. 2012), $\sin^2 \theta_{13} = 0.0236 \pm 0.0042(\text{stat}) \pm 0.0013(\text{sys})$ (Daya Bay Collaboration, F. P. An et al. 2012), and $\sin^2 \theta_{13} = 0.0291 \pm 0.0035(\text{stat}) \pm 0.0051(\text{sys})$ (RENO Collaboration, J. K. Ahn et al. 2012). The latter two results, because of their precision, effectively remove a degree of freedom from three-flavor solar neutrino analyses.

The mass differences and mixing angles from the global analyses of the Bari (Fogli et al. 2012) and Valencia (Forero, Tórtola & Valle 2012) groups, including experimental results through the Neutrino 2012 Conference, are shown in Table

3. The two analyses are generally in quite good agreement and yield (in degrees)

$$\theta_{12} \sim \begin{cases} 33.6_{-1.0}^{+1.1} \\ 34.4_{-1.1}^{+1.0} \end{cases} \quad \theta_{13} \sim \begin{cases} 8.96_{-0.51}^{+0.45} & \text{Bari} \\ 9.06_{-0.57}^{+0.50} & \text{Valencia} \end{cases} \quad (40)$$

The agreement in the solar neutrino mass difference δm_{21}^2 is also excellent,

$$\delta m_{21}^2 \sim \begin{cases} (7.54_{-0.22}^{+0.26}) \times 10^{-5} \text{ eV}^2 & \text{Bari} \\ (7.62_{-0.19}^{+0.19}) \times 10^{-5} \text{ eV}^2 & \text{Valencia} \end{cases} \quad (41)$$

The values for θ_{12} and δm_{21}^2 lie in the LMA region of Fig. 6. δm_{21}^2 corresponds, for 10 MeV neutrinos, to an MSW crossing density of $\sim 20 \text{ g/cm}^3$, or equivalently a solar radius of $r \sim 0.24R_\odot$, the outer edge of the Sun's energy-producing core. The crossing density for the atmospheric δm_{31}^2 , again for 10 MeV neutrinos, is $\sim 1.6 \times 10^3 \text{ g/cm}^3$. Thus this crossing requires electron densities far beyond those available in the Sun – though typical of the carbon zone in the mantle of a Type II supernova, where this second crossing plays a significant role.

These global analysis results can be compared with those from the recent SNO three-flavor combined analysis, which used all available solar neutrino data and the results from KamLAND. This analysis, summarized in Fig. 7, gives at 1σ

$$\sin^2 \theta_{12} = 0.308 \pm 0.014 \quad \delta m_{21}^2 = (7.41_{-0.19}^{+0.21}) \times 10^{-5} \text{ eV}^2 \quad \sin^2 \theta_{13} = 0.025_{-0.015}^{+0.018} \quad (42)$$

These values are in excellent agreement with the corresponding 1σ Bari and Valencia results of Table 3: the SNO combined analysis and Bari best values match particularly well. The main consequence of the inclusion of new reactor and accelerator results in the global analyses is a substantial reduction in the uncertainty on θ_{13} .

5.2 Spectral Distortions: LET Analyses and Borexino

Characteristic spectral distortions are one of the signatures of oscillations in matter. Rather fortuitously, if one evaluates Eq. (34) for the neutrino energy where the MSW critical density corresponds to the electron density at the center of the Sun, $\rho \sim 6 \times 10^{25}/\text{cm}^3$, one finds $E_{\text{crit}}^\nu \sim 1.9$ MeV, an energy in the center of the solar neutrino spectrum. Neutrinos below this energy will not experience a level crossing on exiting the Sun, and thus will oscillate approximately as they would in vacuum – an average (two-flavor) survival probability of

$$P_{\nu_e}^{\text{vacuum}} \sim 1 - \frac{1}{2} \sin^2 2\theta_{12} \sim 0.57, \quad (43)$$

using $\theta_{12} \sim 34^\circ$. This can be compared to the matter-dominated survival probability, appropriate for neutrinos much above the critical energy,

$$P_{\nu_e}^{\text{high density}} \rightarrow \sin^2 \theta_{12} \sim 0.31. \quad (44)$$

Most of the ^8B neutrinos studied by SNO and Super-Kamiokande undergo matter-enhanced oscillations. The matter/vacuum transition predicted by the MSW mechanism can be verified by comparing the survival probabilities of low-energy (pp or ^7Be) and high-energy (^8B) neutrinos. Alternatively, if the thresholds in SNO and Super-Kamiokande are lowered sufficiently, spectral distortions will be detectable in the ^8B spectrum: low-energy ^8B neutrinos coming from the outer core will not experience a crossing, and thus will have a higher survival rate.

The flux of low-energy pp neutrinos is well constrained in global analyses because these neutrinos dominate the SAGE and GALLEX/GNO counting rates. (The need for an elevated survival probability for these neutrinos was an important factor in early model-independent analyses that concluded undistorted neutrino fluxes could not account for the data.) Furthermore Borexino has now

provided a direct, exclusive measurement at a precise energy, corresponding to the 860 keV neutrinos from ${}^7\text{Be}$ electron capture.

To probe lower energy ${}^8\text{B}$ neutrinos, a joint re-analysis of Phase I and Phase II data from the Sudbury Neutrino Observatory was carried out with an effective kinetic energy threshold of $T_{\text{eff}} = 3.5$ MeV (SNO Collaboration, B. Aharmim et al. 2010). While the low-energy threshold analysis (LETA) had several motivations (e.g., the enlarged data set improved the overall precision of the flux determinations), a principal goal was enhancing prospects for detection of the predicted upturn in P_{ν_e} with decreasing neutrino energy. An effort similar to the LETA analysis is now underway in Super-Kamiokande IV: preliminary results were recently described by Smy (2012).

Figure 8 summarizes the data. The pattern defined by the pp ν_e flux deduced from global analyses, the ${}^7\text{Be}$ ν_e flux derived from the Borexino ES measurement, and the SNO results are generally in good agreement with the expected MSW survival probability. However, while the SNO LETA band is compatible with the MSW prediction, the band's centroid trends away from the theory with decreasing energy.

5.3 Day-Night Differences

Two sources of time variation in neutrino rates are the annual $\sim 7\%$ modulation associated with the 1.7% eccentricity in the Earth's orbit around the Sun, and the daily variation associated with terrestrial matter effects, which influence the night-time flux of up-going neutrinos. Both effects have been the subject of careful experimental studies: see, e.g., SNO Collaboration, B. Aharmim et al. (2005); Super-Kamiokande Collaboration, M. B. Smy et al. (2004). The integrated day-

night asymmetry in neutrino detection rates

$$A_{\text{DN}} \equiv \frac{R_{\text{D}} - R_{\text{N}}}{\frac{1}{2}(R_{\text{D}} + R_{\text{N}})}, \quad (45)$$

where R_{D} and R_{N} denote the day and night rates, is the quantity most often studied to assess matter effects associated with solar neutrino passage through the Earth. In principle, similar differential quantities could be defined as functions of the neutrino energy and zenith angle. However, the detection of even the integrated difference A_{DN} is statistically challenging, as the effect is expected to be only a few percent.

A_{DN} provides an “on-off” test where the matter effects can be measured directly, unlike the solar case where matter effects must be deduced from phenomena such as spectral distortions. The magnitude of the neutrino regeneration associated with passage through the Earth depends on the neutrino energy, the assumed oscillation parameters, and, to some extent, detector location, as that determines the possible trajectories through the Earth to the Sun.

The high counting rate of Super-Kamiokande is an advantage in constraining the contribution to A_{DN} from the high-energy ${}^8\text{B}$ neutrinos. The expected Super-Kamiokande ES A_{DN} is illustrated in Fig. 9 as a function of δm_{21}^2 and $\sin^2 \theta_{13}$, in the two- and three-flavor cases. For the current global best-fit parameters, the effect should be about -3% . The results for the four phases

$$\begin{aligned} -2.1 \pm 2.0 \pm 1.3\% \quad \text{SK I} & \quad 6.3 \pm 4.2 \pm 3.7\% \quad \text{SK II} \\ -5.9 \pm 3.4 \pm 1.3\% \quad \text{SK III} & \quad -5.2 \pm 2.3 \pm 1.4\% \quad \text{SK IV (preliminary)} \end{aligned} \quad (46)$$

yield a combined result of $A_{\text{DN}}^{\text{ES}}(\text{SK}) = -4.0 \pm 1.3 \pm 0.8$, in good agreement with expectations but still consistent with no effect at 2.6σ (Smy 2012).

The SNO Collaboration has analyzed day-night effects in the ν_e channel in

their combined analysis, approximating the effect as linear in E_ν ,

$$A_{\text{DN}}^{\nu_e}(\text{SNO}) = -a_0 - a_1 \left(\frac{E_\nu}{10 \text{ MeV}} - 10 \right). \quad (47)$$

The null hypothesis that there are no day/night effects influencing the ν_e survival probability (so $a_0 = 0$, $a_1 = 0$) yielded a $\Delta\chi^2 = 1.87$ (61% c.l.) compared to the best fit (SNO Collaboration, B. Aharmim et al. 2012). The Borexino result for the ES at 862 keV (Borexino Collaboration, G. Bellini et al. 2012b),

$$A_{\text{DN}}^{\text{ES}}(862 \text{ keV}) = -(0.001 \pm 0.012 \pm 0.007), \quad (48)$$

is consistent with the expectation that $|A_{\text{DN}}^{\text{ES}}(862 \text{ keV})| \lesssim 0.001$ for the LMA solution at this energy.

6 NEUTRINO CONSTRAINTS ON SOLAR STRUCTURE

One of the important consequences of the increasingly precise understanding of neutrino flavor physics is the opportunity to return to one of the early goals of solar neutrino spectroscopy, using the neutrino as a probe of the physics of the solar interior. Neutrino fluxes, sensitive to nuclear reaction rates and core temperature, can be combined with helioseismic observations, sensitive to radiative opacities and microscopic diffusion, to place stringent constraints on the SSM and to test some of its implicit assumptions. This program is of broad significance to stellar astrophysics because the SSM is a particular application of the general theory of main-sequence stellar evolution. Because we know the Sun's properties far better than those of any other star, the SSM provides one of our best opportunities to test that theory against precise data, and thus to identify shortcomings.

A decade ago the SSM was in spectacular agreement with observations apart

from solar neutrino data, a fact that supported suggestions that the solar neutrino problem might have a nonsolar origin. However, as the SSM makes a number of simplifying assumptions, it is perhaps inevitable that some experimental test of our Sun will eventually demonstrate the model’s shortcomings. Over the past decade, the development of 3D hydrodynamic models of near-surface solar convection, a more careful selection of spectral lines, and, in some cases, relaxation of the assumption of local thermodynamic equilibrium in line formation have led to significant changes in the analysis of data on photospheric absorption lines. The most recent revisions reduced the abundances of the volatile CNO elements and Ne by ~ 0.10 - 0.15 dex (equivalently, by $\sim 25 - 40\%$), relative to older compilations of solar abundances – though significant debate continues. The differences between the new AGSS09 and the older GS98 abundances can be summarized in the respective total-metal-to-hydrogen ratios of $(Z/X)_{\odot} \sim 0.018$ and 0.023 , respectively. As the SSM assumes a homogeneous zero-age composition, adoption of the AGSS09 abundances produces a modern Sun with a lower core metallicity, affecting solar neutrino flux predictions and substantially degrading the agreement between the SSM sound velocity profile and that deduced from helioseismology.

6.1 The Solar Abundance Problem and its SSM Implications

Past studies of SSMs with low Z/X interiors similar to that of the AGSS09-SFII SSM have revealed a number of difficulties with respect to observation: the radius of the convective zone boundary R_{CZ} , the interior sound speed and density profiles, and the surface He abundance Y_S all move outside the ranges determined from helioseismic analyses (Bahcall, Serenelli & Pinsonneault 2004; Basu & Antia 2004; Montalbán et al. 2004). These changes reflect the increase in

the efficiency of radiative transport and decrease in core molecular weight found in low- Z models. For example, R_{CZ} moves outward in low- Z models because radiative transport dominates over a larger fraction of the solar interior. Similarly, Y_S decreases: As SSM energy generation is fixed by the measured luminosity L_{\odot} , the cooler core in low- Z models must be compensated by an increase in the available fuel X , and consequently a lower core Y and thus surface Y_S . In contrast, SSM predictions using the older, high- Z GS98 abundances are in much better agreement with observation. (See Table 1 and Fig. 5.) The inconsistency between the SSM parameterized using the best current description of the photosphere (AGSS09 abundances) and the SSM parameterized to optimize agreement with helioseismic data sensitive to interior composition (GS98 abundances) is known as the solar abundance problem.

The solar abundance problem could have a pedestrian solution: the 3D analysis of Caffau et al. (2008, 2009, 2010) yielded abundances higher than the AGSS09 values, though this appears to be due to spectral line choices rather than photospheric model differences (Grevesse et al. 2011), a conclusion supported by a recent comparison between solar model atmospheres computed by different groups (Beeck et al. 2012). Alternatively, an upward adjustment in associated atomic opacities could compensate for a low- Z interior, if some justification for such a change could be identified.

However, the solar abundance problem could be more fundamental. An important assumption of the SSM – a homogeneous zero-age Sun – is not based on observation, but instead on the theoretical argument that the proto-Sun likely passed through a fully convective Hayashi phase as the pre-solar gas cloud collapsed, thereby destroying any composition inhomogeneities that might have ex-

isted. Yet we know that chemical inhomogeneities were re-established during solar system formation: processes operating in the proto-planetary disk removed $\sim 40 - 90M_{\oplus}$ of metal from the gas, incorporating this material in the gaseous giants (Guillot 2005). The gas from which these metals were scoured – representing perhaps the last $\sim 5\%$ of that remaining in the disk – would have been depleted in metal, and enriched in H and He. The fate of that gas is unknown, but if it were accreted onto the Sun, it plausibly could have altered the composition of the convective zone, depending on the timing of the accretion and thus the maturity of the proto-Sun’s growing, chemically segregated radiative core. That is, as there is a candidate mechanism for altering the convective zone late in proto-solar evolution, involving enough metal to account for the AGSS09/GS98 differences, it is not obvious that the SSM assumption of homogeneity is correct.

The solar abundance problem has three connections to neutrinos:

1. Neutrino fluxes are sensitive to metallicity, and thus can be used to cross-check the conclusions drawn from helioseismology. Below we describe what the neutrino fluxes currently tell us.
2. Neutrino fluxes place important constraints on nonstandard solar models (NSSMs) motivated by the solar abundance problem, such as those recently developed to explore accretion from the proto-planetary disk.
3. Planned measurements (Chen 2006, Franco 2011) of the CN solar neutrino flux have the potential to directly measure the solar core abundance of C+N with a precision that will impact the solar abundance problem.

In principle the temperature-dependent ^8B and ^7Be neutrino fluxes have sufficient sensitivity to metallicity to impact the solar abundance debate. As Table 2 shows, the AGSS09-SFII and GS98-SFII SSMs differ by 21.6% and 9.6% in their

^8B and ^7Be flux predictions, respectively, which one can compare to the 14% and 7% SSM uncertainties on these fluxes obtained by varying SSM input parameters according to their assigned errors. These total SSM uncertainties were determined by adding in quadrature the individual uncertainties from 19 SSM input parameters, including abundance uncertainties as given in the respective solar abundance compilations. In the case of the ^8B flux, the important uncertainties include those for the atomic opacities (6.9%), the diffusion coefficient (4%), the nuclear S-factors for $^3\text{He}+^4\text{He}$ (5.4%) and $^7\text{Be}+\text{p}$ (7.5%), and the Fe abundance (5.8%).

Unfortunately the current neutrino data do not favor either abundance set. The last entries in Table 2 give the χ^2 functions and compatibility functions P^{agr} obtained in the SSM for the two sets, following Gonzales-Garcia, Maltoni & Salvado (2010) but using the updated Solar Fusion II S-factors. The two models are identical in quality of fit to the data, with $\chi^2_{\text{AGSS09-SFII}} = 3.4$ and $\chi^2_{\text{GS98-SFII}} = 3.5$. From Table 2 one sees that a SSM model intermediate in metallicity between AGSS09 and GS98 would optimize the agreement.

6.2 Solar Models with Accretion

Guzik (2006), Castro, Vauclair & Richard (2007), and Guzik & Mussack (2010) considered the possibility that the solar abundance problem might be due to accretion of metal-poor matter onto the Sun's convective envelope, diluting its pre-solar composition. Haxton & Serenelli (2008) suggested the mechanism for such dilution described above, accretion of disk gas from which the metals were previously scoured in the process of planetary formation. Evidence supporting the hypothesis that planet formation could affect the surface metallicity of the

host star was offered by Melendez et al. (2009), who found that the peculiar differences in the surface abundances of the Sun, measured relative to similar stars (solar twins), correlate with condensation temperatures, and thus plausibly with disk chemistry. Nordlund (2009) argued this accretion scenario might also provide a natural explanation for the anomalous metallicity of Jupiter.

While the process of planetary formation is not well understood, the standard picture invokes a chemically differentiated thin disk, with dust, ice, and thus metals concentrated in the midplane, and outer surfaces dominated by H and He. This configuration arises from a combination of gas cloud collapse that is rapid at the poles but inhibited by angular momentum at the equator, and gas cooling that allows differential condensation of various elements as ice or grains according to their condensation temperatures. The formation of planetesimals in the midplane and their self-interactions lead to the formation of rocky cores of planets. The gas giants, which are sufficiently distant from the Sun that ice can augment their cores, reach masses where tidal accretion of gas can further feed their growth.

The implications of this disk chemistry for solar initial conditions is difficult to assess because of a number of uncertain parameters. While we know the planets are substantial metal reservoirs, we do not know the fate of the depleted gas that dominates the disk surface: it might have been removed by the solar wind, or alternatively deposited on the Sun through magnetospheric mechanisms, such as those operating in young accreting T Tauri stars. If accretion occurs, its timing relative to early solar evolution is critical. The timescale for planetary formation is generally estimated at 1-10 M.y., while the SSM predicts that the early Sun's convective boundary moves outward, in response to the growing radiative core,

over a longer period of $\tau_{CZ} \sim 30$ M.y. If accretion occurs early in this period, when most of the Sun’s mass is in its convective envelope, any resulting nonuniformity in solar abundances would be negligible. But if accretion occurs later when the convective zone is similar to that of the modern Sun, and thus contains only $\sim 2\%$ of the Sun’s mass, the chemical processing of $\sim 0.05M_{\odot}$ of gas, dust, and ice in the planetary nebula could have very significant consequences. Alternatively, as suggested by hydrodynamic simulations of the contraction of the protosolar nebula (Wuchterl & Klessen 2001) and stellar models that include episodic accretion during the pre-main-sequence phase with large mass accretion rates (Baraffe & Chabrier 2010), the Sun may have avoided the fully convective phase altogether. Finally, the mass and composition of the accreted material is highly uncertain. Because condensation temperatures for the elements vary widely – e.g., from ~ 1400 K for Fe to ~ 300 K for C – the composition would likely evolve with time as the disk cools.

Motivated in part by such considerations, a NSSM was recently developed to test whether early accretion from a planetary disk could resolve the solar abundance problem (Serenelli, Haxton & Peña-Garay 2011). The work illustrates the importance of neutrino physics in limiting NSSMs. In SSMs the pre-solar composition parameters Y_{ini} and Z_{ini} as well as the mixing length parameter α_{MLT} are determined by iterating the model to reproduce the present-day solar luminosity L_{\odot} , radius R_{\odot} , and surface metal-to-hydrogen ratio Z_S/X_S . This algorithm was modified for the accreting NSSM by allowing for a mass M_{ac} of accreted material with fixed composition $(X_{\text{ac}}, Y_{\text{ac}}, Z_{\text{ac}})$, deposited on the early Sun uniformly, beginning at time $\tau_{\text{ac},i}$ and lasting a time $\Delta\tau_{\text{ac}}$. Prior to time $\tau_{\text{ac},i}$ the Sun was evolved as a SSM with mass $M_{\odot} - M_{\text{ac}}$ and composition defined by $(X_{\text{ini}},$

$Y_{\text{ini}}, Z_{\text{ini}}$). During the subsequent accretion phase, the simplifying assumption $X_{\text{ac}}/Y_{\text{ac}} \equiv X_{\text{ini}}/Y_{\text{ini}}$ was made. For a given set of fixed accretion parameters, $Y_{\text{ini}}, Z_{\text{ini}}$, and α_{MLT} were then adjusted iteratively in order to reproduce L_{\odot} , R_{\odot} , and Z_S/X_S , as in the SSM. Thus $Y_{\text{ini}}, Z_{\text{ini}}$, and α_{MLT} become functions of the assumed accretion parameters, so that in place of a single SSM solution, a family of solutions is obtained with different interior compositions. Unphysical solutions are rejected, e.g., the AGSS09 Z_S/X_S is not compatible with the accretion of large quantities of metal-rich material at late times, when the convective envelope is thin.

Fig. 10 shows the helioseismic consequences of late accretion – accretion onto a young Sun with a thin convective envelope similar to that of the modern Sun. Also shown are the variations in Y_{ini} and Z_{ini} , the initial core He and heavy-element mass fractions, that can be achieved through accretion. The helioseismic observables are very constraining. The candidate accretion solution to the solar abundance problem that one might naively envision – a low- Z surface consistent with AGSS09 and an interior similar to GS98, with higher $Z_{\text{ini}} \sim 0.019$ and $Y_{\text{ini}} \sim 0.28$ – can be achieved with metal-free and metal-poor accretion involving modest accreted masses $M_{\text{ac}} \sim 0.01M_{\odot}$. These models bring Y_S into good agreement with observation and produce some improvement in the sound-speed figure-of-merit $\langle \delta c/c \rangle$. But the lower Z_S that accompanies metal-free/metal-poor accretion allows the convective zone radius to move outward, exacerbating the existing AGSS09-SFII SSM helioseismic discrepancy in R_S .

Neutrino flux measurements impose a second class of constraints on accreting NSSMs. The scenario discussed above – metal-free or metal-poor accretion with $M_{\text{ac}} \sim 0.01M_{\odot}$ – can marginally improve the agreement with experiment, con-

sistent with earlier observations that this produces an interior similar to GS98, and that the GS98 and AGSS09 SSMs yield equivalent fits to the solar neutrino data. But with larger M_{ac} the agreement quickly deteriorates as the resulting high-Z interior leads to rapid increases in the ^8B and ^7Be neutrino fluxes. The power of contemporary neutrino flux measurements to constrain NSSMs is quite remarkable. Large classes of accretion parameters – mass, time, composition, and duration – lead to modern Suns with the proper luminosity and radius and the AGS009 Z_S , while satisfying the underlying equations of stellar structure. Yet very few of these solutions produce acceptable neutrino fluxes, as Fig. 11 illustrates.

Effectively the recent progress made on neutrino mixing angles and mass differences has made the neutrino into a well understood probe of the Sun. We now have two precise tools, helioseismology and neutrinos, that can be used to see into the solar interior, complementing the more traditional astronomy of solar surface observations. Effectively we have come full circle: the Homestake experiment was to have been a measurement of the solar core temperature, until the solar neutrino problem intervened.

6.3 Neutrinos as a Direct Probe of Solar Composition: SNO+

While solar fusion is dominated by the pp chain, the CN cycle generates $\sim 1\%$ of solar energy as well as ^{13}N and ^{15}O neutrino fluxes of 2.96 (2.17) and 2.23 (1.56) $\times 10^8/\text{cm}^2\text{s}$, respectively, for the GS98-SFII (AGSS09-SFII) SSM. These fluxes can be measured in scintillation detectors in an energy window of 800-1400 keV, provided backgrounds in the detectors are reduced to acceptable levels, including in particular interference from the decay of ^{11}C produced by penetrating

muons. Borexino has already established a limit on the CN fluxes, and is pursuing strategies to improve the measurement by vetoing interfering backgrounds (Franco 2011). A new scintillation detector under construction in the cavity previously occupied by SNO will have three times the volume of Borexino and 1/70th the muon background, due to SNOLab’s two-kilometer depth (Chen 2006). A SNO+ CN neutrino signal/ ^{11}C background of ~ 10 is expected.

A measurement of the CN neutrinos would test our understanding of hydrogen fusion as it occurs in main-sequence stars substantially more massive than the Sun. It could also play an important role in the solar abundance problem.

The CN neutrino fluxes, like the ^8B and ^7Be neutrino fluxes, depend sensitively on core temperature T_C and thus respond to variations in SSM input parameters that affect T_C . But in addition, the CN fluxes have a linear dependence on the pre-solar core abundances of C and N that is unrelated to T_C , reflecting the proportionality of CN neutrino fluxes to the abundances that catalyze the hydrogen burning. The T_C power-law relationships for the CN and ^8B neutrino fluxes and the additional linear dependence of the CN neutrino flux on the abundance of C+N can be exploited to relate solar neutrino measurements to the Sun’s pre-solar C and N abundances (Haxton & Serenelli 2008)

$$\frac{\phi(^{15}\text{O})}{\phi(^{15}\text{O})_{\text{SSM}}} = \left[\frac{\phi(^8\text{B})}{\phi(^8\text{B})_{\text{SSM}}} \right]^{0.729} x_{C+N} \times [1 \pm 0.006(\text{solar}) \pm 0.027(\text{D}) \pm 0.099(\text{nucl}) \pm 0.032(\theta_{12})] \quad (49)$$

where x_{C+N} is the C+N number abundance normalized to its SSM value. The uncertainties were derived from SSM logarithmic derivatives, as described in Sec. 2. The first two of these represent variations in all SSM parameters other than the nuclear cross sections – including L_\odot , the opacity, solar age, and all abundances

other than C and N, using abundance uncertainty intervals of

$$x_j \equiv 1 \pm \left| \frac{\text{Abundance}_i^{\text{GS98}} - \text{Abundance}_i^{\text{AGSS09}}}{(\text{Abundance}_i^{\text{GS98}} + \text{Abundance}_i^{\text{AGSS09}})/2} \right|. \quad (50)$$

Apart from the diffusion parameter D , the net effect of the variations in these quantities is an uncertainty of 0.6%: we have formed a ratio of fluxes that is effectively insensitive to T_C . The diffusion parameter D is an exception because our expression relates contemporary neutrino flux measurements to the pre-solar number densities of C and N, and thus must be corrected for the effects of diffusion over 4.6 Gy. The differential effects of diffusion on the ratio creates an uncertainty of 2.7%, the only significant nonnuclear solar uncertainty.

Equation (49) is written for instantaneous fluxes, and thus must be corrected for the energy-dependent effects of oscillations. The SNO combined analysis result $\theta_{12} = 34.06_{-0.84}^{+1.16}$ – or equivalently the Bari or Valencia global analysis results of Sec. 5 – imply a $\lesssim 3.2\%$ uncertainty in the flux comparison of Eq. (49). Finally, there are nuclear physics uncertainties. These dominate the overall error budget, with the combined (in quadrature) error reflecting a 7.2% uncertainty from the $^{14}\text{N}(p,\gamma)$ reaction and a 5.5% uncertainty from $^7\text{Be}(p,\gamma)$.

The SNO and Super-Kamiokande measurements of the ^8B flux have reached a precision of 3%. SNO+ has the potential to measure the ^{15}O flux to about 7% in three years of running. Assuming such a result from SNO+ and combining all errors in quadrature, one finds that the pre-solar C+N abundance can be determined to $\pm 13\%$. The precision could be improved substantially by addressing the uncertainties in the S-factors S_{114} and S_{17} . But even without such improvements, the envisioned SNO+ result would have a major impact, given the existing $\sim 30\%$ differences in the AGSS09 and GS98 C and N abundances.

7 OUTLOOK AND CHALLENGES

In this review we have summarized the results of 50 years of work on solar neutrinos. The field has been characterized by very difficult experiments carried out with great success, producing results fundamental to two standard models, our standard theory of stellar evolution and our standard model of particle physics. Thirty years of debate over the origin of the solar neutrino problem – a misunderstanding of the structure of the Sun, or an incomplete description of the properties of the neutrino – ended with the discovery of massive neutrinos, flavor mixing, and MSW distortions of the solar neutrino spectrum. The quest to resolve the solar neutrino problem spurred the development of a new generation of active detectors of unprecedented volume and radiopurity – SNO, Super-Kamiokande, and Borexino – that have made solar neutrino spectroscopy a precise science. This technology has opened up new possibilities.

The program of solar neutrino studies envisioned by Davis and Bahcall has been only partially completed. Borexino has extended precision measurements to low-energy solar neutrinos, determining the flux of ${}^7\text{Be}$ neutrinos to 5%, and thereby confirming the expected increase in the ν_e survival probability for neutrino energies in the vacuum-dominated region. First results on the pep neutrino flux have been obtained, as well as a limit on the CN neutrino fluxes. But a larger, deeper version of Borexino, SNO+, will likely be needed to map out the low-energy solar neutrino spectrum in detail, including the CN neutrino contributions. The observation of these neutrinos in the Sun would provide an important test of the nuclear reactions we believe dominate energy generation in massive hydrogen-burning stars.

There are challenging tasks remaining. The flux of solar pp neutrinos, known

theoretically to $\pm 1\%$, is our most accurately predicted source of ν_e s. The detection of these neutrinos (Grieb et al. 2011) would check the luminosity condition so widely used in solar neutrino analyses, the equivalence of solar energy production as measured in emitted photons to that deduced from the neutrinos – a test also relevant to possible new physics, such as sterile neutrinos (Abazajian et al. 2012). The pp neutrinos could also provide our most precise low-energy normalization for calibrating the MSW effects that turn on with increasing energy. We have discussed the excellent prospects that SNO+, by measuring the ^{15}O CN neutrinos (1.73 MeV endpoint), will directly determine the pre-solar C+N content of the solar core to a precision that will impact the solar abundance problem. Though a much more challenging task, the measurement of the lower energy ^{13}N neutrinos (1.20 MeV endpoint) to high precision could yield separate determinations of the core C and N abundances: the $\sim 35\%$ higher flux of ^{13}N neutrinos reflects the ongoing burning of pre-solar carbon in the Sun’s cooler outer core, as discussed in Sec. 2. Finally, there is the next-to-next-generation challenge of measuring the Sun’s thermal neutrinos (Haxton & Lin 2000), a solar source that becomes significant below 10 keV, with a peak flux density of $\sim 10^9/\text{cm}^2/\text{s}/\text{MeV}$. Neutrinos of all flavors are produced by various $Z_0 \rightarrow \nu\bar{\nu}$ processes operating in the Sun. Their fluxes are a sensitive thermometer for the solar core, independent of nuclear physics, and depend on the core abundance of Fe and other heavy elements, due to the contribution of free-bound transitions where a Z_0 is radiated. The most likely candidate for detection may be the $\bar{\nu}_e$ s, as the correspondence between thermal neutrino energies and typical inverse atomic scales suggests some form of resonant absorption process.

In retrospect, it is remarkable that we have learned so much fundamental

physics from an object as manifestly complicated as the Sun – with all of its 3D physics, magnetic fields, convective and radiative transport, and nontrivial nuclear and atomic physics. Apart from improving the precision of input parameters and small tweaks in the physics, such as the inclusion of He and heavy element diffusion, the SSM that helped us extract new neutrino physics from the Sun is the same model Bahcall, Fowler, Iben, and Sears employed in 1963 to make the first prediction of solar neutrino fluxes. It would not be surprising to see cracks finally appearing in that model, under the relentless pressure of experiments measuring neutrino fluxes with few percent precision and helioseismic mappings of interior sound speeds to a few parts in a thousand.

We have reviewed one possible crack in some detail – the solar abundance problem. Despite the lack of consensus on this issue, it has raised an interesting question: why have we done so well with a model that assumes a homogeneous zero-age Sun, when the large-scale segregation of metals is apparent from planetary structure? The abundance problem has been linked to dynamical issues in the collapse of the solar nebula, the metallicity of solar twins, and the anomalous composition of Jupiter. We also have seen that neutrinos could provide a crucial check on the possibility of an inhomogeneous Sun because of the sensitivity of the CN neutrino flux to the C+N content of the core. It could well turn out that we are encountering the first evidence that a more complete model is needed – perhaps one that moves beyond an isolated Sun, to address the chemical and dynamical coupling of the Sun and planets at their births. Just as the SSM allowed us to exploit our best understood star to test the general theory of main-sequence stellar evolution, an effort to develop a Standard Solar System Model – one with gas cloud collapse, disk formation and accretion, realistic pre-solar evolution,

the growth of planets, and the coupled astrochemistry of the Sun and planets – could provide a needed template for interpreting what we are now learning about exoplanets and their host stars.

We are very grateful to Michael Smy for several helpful discussions on Super-Kamiokande. This work was supported in part by the US Department of Energy under contracts DE-SC00046548 (UC Berkeley), DE-AC02-98CH10886 (LBNL), and DE-FG02-97ER41020 (CENPA, Univ. Washington). AS is partially supported by the European Union International Reintegration Grant PIRG-GA-2009-247732, the MICINN grant AYA2011-24704, the ESF EUROCORES Program EuroGENESIS (MICINN grant EUI2009-04170), the SGR grants of the Generalitat de Catalunya, and EU-FEDER funds.

8 LITERATURE CITED

References

- Abazajian KN, et al. 2011. *Astropart. Phys.* 35:177
- Abazajian KN, et al. 2012. arXiv:1204.5379
- Adelberger EG, et al. 1998. *Rev. Mod. Phys.* 70:1275
- Adelberger EG, et al. 2011. *Rev. Mod. Phys.* 83:195
- Akhmedov EK. 1988. *Phys. Lett. B* 213:64
- Alvarez LW. 1949. Lawrence Rad. Lab. Phys. Notes Memo #767
- Appourchaux T, Belkacem K, Broomhall AM, Chaplin WJ, Gough DO, et al. 2010. *A&A Rev.* 18:197
- Asplund M, Grevesse N, Sauval AJ, Scott P. 2009. *Ann. Rev. Astron. Astrophys.* 47:481

- Bahcall JN. 1964. *Phys. Rev. Lett.* 12:300
- Bahcall JN. 1989. *Neutrino Astrophysics*. Cambridge University Press
- Bahcall JN, Bahcall NA, Shaviv G. 1968. *Phys. Rev. Lett.* 20:1209
- Bahcall JN, Cabibbo N, Yahil A. 1972. *Phys. Rev. Lett.* 28:316
- Bahcall JN, Davis Jr. R. 1982. In *Essays in Nuclear Astrophysics*, eds. CA Barnes, DD Clayton, D Schramm. Cambridge University Press, 243–285
- Bahcall JN, Fowler WA, Iben I, Sears RL. 1963. *Ap. J.* 1237:344
- Bahcall JN, Krastev PI, Smirnov AY. 1998. *Phys. Rev. D* 58:096016
- Bahcall JN, Peña-Garay C. 2003. *JHEP* 11:004
- Bahcall JN, Pinnsoneault MH. 1995. *Rev. Mod. Phys.* 67:781
- Bahcall JN, Pinsonneault MH. 1992. *Rev. Mod. Phys.* 64:885
- Bahcall JN, Serenelli AM, Pinsonneault M. 2004. *Ap. J.* 614:464
- Baraffe I, Chabrier G. 2010. *A&A* 521:A44
- Basu S, Antia HM. 1997. *MNRAS* 287:189
- Basu S, Antia HM. 2004. *Ap. J.* 606:L85
- Basu S, Chaplin WJ, Elsworth Y, New R, Serenelli AM. 2009. *Ap. J.* 699:1403
- Beeck B, Collet R, Steffen M, Asplund M, Cameron RH, et al. 2012. *A&A* 539:A121
- Bethe HA. 1986. *Phys. Rev. Lett.* 56:1305
- Blennow M, Ohlsson T, Snellman H. 2004. *Phys. Rev. D* 69:073006
- Bonetti R, et al. 1999. *Phys. Rev. Lett.* 82:5205
- Borexino Collaboration, G. Alimonti et al. 2009. *Nucl. Instrum. Meth. A* 600:568

- Borexino Collaboration, G. Bellini et al. 2010. *Phys. Rev. D* 82:033006
- Borexino Collaboration, G. Bellini et al. 2011. *Phys. Rev. Lett.* 107:141302
- Borexino Collaboration, G. Bellini et al. 2012a. *Phys. Rev. Lett.* 108:051302
- Borexino Collaboration, G. Bellini et al. 2012b. *Phys. Lett. B* 707:22
- Caffau E, et al. 2008. *Astron. Astrophys.* 488:1031
- Caffau E, et al. 2009. *Astron. Astrophys.* 498:877
- Caffau E, et al. 2010. *Astron. Astrophys.* 514:A92
- Cameron AGW. 1958. *Ann. Rev. Nucl. Sci.* 8:299
- Castellani V, Degl'Innocenti S, Fiorentini G, Lissia M, Ricci B. 1994. *Phys. Rev. D* 50:4749
- Castro M, Vauclair S, Richard O. 2007. *A&A* 463:755
- Chaplin WJ, Miglio A. 2013. To be published in *Ann. Rev. Astron. Astrophys.*, vol. 51
- Chen HH. 1985. *Phys. Rev. Lett.* 55:1534
- Chen M. 2006. *AIP Conf. Proc.* 944:25
- Christensen-Dalsgaard J. 2002. *Rev. Mod. Phys.* 74:1073
- Davis Jr. R. 1955. *Phys. Rev.* 97:766
- Davis Jr. R. 1964. *Phys. Rev. Lett.* 12:303
- Davis Jr. R, Harmer DS, Hoffman KC. 1968. *Phys. Rev. Lett.* 20:1205
- Daya Bay Collaboration, F. P. An et al. 2012. *Phys. Rev. Lett.* 108:171803
- Dilke JFWW, Gough DO. 1972. *Nature* 240:262
- Double Chooz Collaboration, Y. Abe et al. 2012. *Phys. Rev. Lett.* 108:131801

- Duebner FL, Gough D. 1984. *Ann. Rev. Astron. Astrophys.* 22:593
- Elliott JR, Kosovichev AG. 1998. *Ap. J.* 500:L199
- Faulkner J, Gilliland RL. 1985. *Ap. J.* 299:994
- Fogli GL, Lisi E, Montanino D, Palazzo A. 2000. *Phys. Rev. D* 62:013002
- Fogli GL, et al. 2012. *Phys. Rev. D* 86:013012
- Forero DV, Tórtola M, Valle JWF. 2012. arXiv:1205.4018v3
- Fowler WA. 1958. *Ap. J.* 127:551
- Franco D. 2011. *Nucl. Phys. B Proc. Suppl.* 221:344
- GALLEX Collaboration, P. Anselmann et al. 1992. *Phys. Lett. B* 285:376
- GALLEX Collaboration, P. Anselmann et al. 1994. *Phys. Lett. B* 327:377
- GALLEX Collaboration, W. Hampel et al. 1999. *Phys. Lett. B* 447:127
- Gavrin VN, Gorbachev VV, Verentekin EP, Cleveland BT. 2011. arXiv:1006.2103
- Gell-Mann M, Ramond P, Slansky R. 1979. In *Supergravity*, eds. D Freedman, P van Nieuwenhuizen. North Holland, 315
- Gizon L, Birch AC. 2005. *Living Rev. Solar Phys.* 2:6
- Gonzales-Garcia MC, Maltoni M, Salvado J. 2010. *JHEP* 1005:072
- Grevesse N, Asplund M, Sauval AJ, Scott P. 2011. *Can. J. Phys.* 89:327
- Grevesse N, Sauval AJ. 1998. *Space Sci. Rev.* 85:161
- Grieb C, et al. 2011. *Nucl. Phys. Proc. Suppl.* 221:349
- Guillot T. 2005. *Ann. Rev. Earth Planetary Sci.* 33:493
- Guzik JA. 2006. In *Proceedings of SOHO 18/GONG 2006/HELAS I, Beyond the Spherical Sun*, vol. 624. ESA, 17

- Guzik JA, Mussack K. 2010. *Ap. J.* 713:1108
- Hata N, Bludman S, Langacker P. 1994. *Phys. Rev. D* 49:3622
- Hata N, Langacker P. 1994. *Phys. Rev. D* 48:2937
- Haxton WC. 1986. *Phys. Rev. Lett.* 57:1271
- Haxton WC. 1995. *Ann. Rev. Astron. Astrophys.* 33:459
- Haxton WC. 2010. *Ann. Rev. Nucl. Part. Sci.* 59:1
- Haxton WC, Lin W. 2000. *Phys. Lett. B* 486:263
- Haxton WC, Serenelli AM. 2008. *Ap. J.* 687:678
- Haxton WC, Zhang WM. 1991. *Phys. Rev. D* 43:2484
- Heeger K, Robertson RGH. 1996. *Phys. Rev. Lett.* 77:3720
- Holmgren HP, Johnston R. 1958. *Bull. Am. Phys. Soc. II* 3:26
- Holmgren HP, Johnston R. 1959. *Phys. Rev.* 113:1556
- Jelley N, McDonald AB, Robertson RGH. 2009. *Ann. Rev. Nucl. Part. Sci.* 59:431
- Kaether F, Hampel W, Heusser G, Kiko J, Kirsten T. 2010. *Phys. Lett. B* 685:47
- Kamiokande Collaboration, K. S. Hirata et al. 1989. *Phys. Rev. Lett.* 63:16
- Kamiokande Collaboration, Y. Fukuda et al. 1996. *Phys. Rev. Lett.* 77:1683
- KamLAND Collaboration, A. Gando et al. 2011. *Phys. Rev. D* 83:052002
- KamLAND Collaboration, S. Abe et al. 2011. *Phys. Rev. C* 84:035804
- KATRIN Collaboration, J. Angrik et al. 2004.
<http://bibliothek.fzk.de/zb/berichte/FZKA7090.pdf>
- Krastev PI, Smirnov AY. 1989. *Phys. Lett. B* 226:341
- Kuzmin VA. 1966. *Sov. Phys. JETP* 22:1051

- Lande K. 2010. *Ann. Rev. Nucl. Part. Sci.* 59:21
- Lim CS, Marciano WJ. 1988. *Phys. Rev. D* 371:1368
- Loreti FN, Balantekin AB. 1994. *Phys. Rev. D* 50:4762
- Maki Z, Nakagawa M, Sakata S. 1962. *Prog. Theor. Phys.* 28:870
- Melendez J, Asplund M, Gustafsson B, Yong D. 2009. *Ap. J.* 704:L66
- Mikheyev SP, Smirnov AY. 1985. *Sov. J. Nucl. Phys.* 42:913
- Mikheyev SP, Smirnov AY. 1986. *Nuovo Cimento* 9C:17
- MINOS Collaboration, P. Adamson et al. 2011. *Phys. Rev. Lett.* 107:181802
- Mohapatra R, Senjanovic G. 1980. *Phys. Rev. Lett.* 44:912
- Montalban J, Miglio A, Noels A, Grevesse N, di Mauro MP. 2004. *SOHO 14 Helio- and Asteroseismology: Towards a Golden Future* 559:574
- Nordlund A. 2009. arXiv:0908.3479
- Otten EW, Weinheimer C. 2008. *Rep. Prog. Phys.* 71:086201
- Parke SJ. 1986. *Phys. Rev. Lett.* 57:1275
- Parke SJ. 1995. *Phys. Rev. Lett.* 74:839
- Peña-Garay C, Serenelli AM. 2008. arXiv:0811.2424
- Pontecorvo B. 1946. Chalk River Report PD-205
- Pontecorvo B. 1967. *Zh. Eksp. Teor. Fiz.* 53:1717
- RENO Collaboration, J. K. Ahn et al. 2012. *Phys. Rev. Lett.* 108:191802
- Rogers FJ, Nayfonov A. 2002. *Ap. J.* 576:1064
- SAGE Collaboration, A. I. Abazov et al. 1991. *Phys. Rev. Lett.* 67:3332
- SAGE Collaboration, J. N. Abdurashitov et al. 1994. *Phys. Lett. B* 328:234

- SAGE Collaboration, J. N. Abdurashitov et al. 2009. *Phys. Rev. C* 80:015807
- Schafer A, Koonin SE. 1987. *Phys. Lett. B* 185:417
- Serenelli AM. 2010. *Astrophys. Space Sci.* 328:13
- Serenelli AM, Basu S, Ferguson JW, Asplund M. 2009. *Ap. J.* 705:L123
- Serenelli AM, Haxton WC, Peña-Garay C. 2011. *Ap. J.* 743:24
- Smy M. 2012. to appear in the Proc. Neutrino 2012
- SNO Collaboration, B. Aharmim et al. 2005. *Phys. Rev. D* 72:052010
- SNO Collaboration, B. Aharmim et al. 2010. *Phys. Rev. C* 81:055504
- SNO Collaboration, B. Aharmim et al. 2012. arXiv:1109.0763 (submitted to *Phys. Rev. C*)
- SNO Collaboration, Q. R. Ahmad et al. 2001. *Phys. Rev. Lett.* 87:071301
- SNO Collaboration, Q. R. Ahmad et al. 2002. *Phys. Rev. Lett.* 89:011301
- Spergel DN, Press WH. 1985. *Ap. J.* 294:663
- Stonehill LC, Formaggio JA, Robertson RGH. 2004. *Phys. Rev. C* 69:015801
- Super-Kamiokande Collaboration. 2012. <http://www-sk.icrr.u-tokyo.ac.jp/sk/index-e.html>
- Super-Kamiokande Collaboration, J. Hosaka et al. 2006. *Phys. Rev. D* 73:112001
- Super-Kamiokande Collaboration, J. P. Cravens et al. 2008. *Phys. Rev. D* 78:032002
- Super-Kamiokande Collaboration, K. Abe et al. 2011. *Phys. Rev. D* 83:052010
- Super-Kamiokande Collaboration, M. B. Smy et al. 2004. *Phys. Rev. D* 69:011104(R)

Super-Kamiokande Collaboration, S. Fukuda et al. 2003. *Nucl. Instrum. Meth.*

A 501:418

Super-Kamiokande Collaboration, Y. Fukuda et al. 1998. *Phys. Rev. Lett.* 81:1562

T2K Collaboration, K. Abe et al. 2011. *Phys. Rev. Lett.* 107:041801

White M, Krauss L, Gates E. 1993. *Phys. Rev. Lett.* 70:375

Wolfenstein L. 1978a. *Phys. Rev. D* 17:2369

Wolfenstein L. 1978b. *Phys. Rev. D* 20:2634

Wuchterl G, Klessen RS. 2001. *Ap. J.* 560:L185

Yanagida T. 1980. *Prog. Theor. Phys.* 64:1103

Table 1: SSM characteristics are compared to helioseismic values, as determined by Basu & Antia (1997, 2004). X, Y, and Z are the mass fractions in H, He, and metals. The subscripts S , C , and ini denote current photospheric, current core, and zero-age values. R_{CZ} is the radius to the convective zone, and $\langle \delta c/c \rangle$ is the average fractional discrepancy in the sound speed, relative to helioseismic values.

Property	GS98	AGSS09	Solar
$(Z/X)_S$	0.0229	0.0178	–
Z_S	0.0170	0.0134	–
Y_S	0.2429	0.2319	0.2485 ± 0.0035
R_{CZ}/R_\odot	0.7124	0.7231	0.713 ± 0.001
$\langle \delta c/c \rangle$	0.0009	0.0037	0.0
Z_C	0.0200	0.0159	–
Y_C	0.6333	0.6222	–
Z_{ini}	0.0187	0.0149	–
Y_{ini}	0.2724	0.2620	–

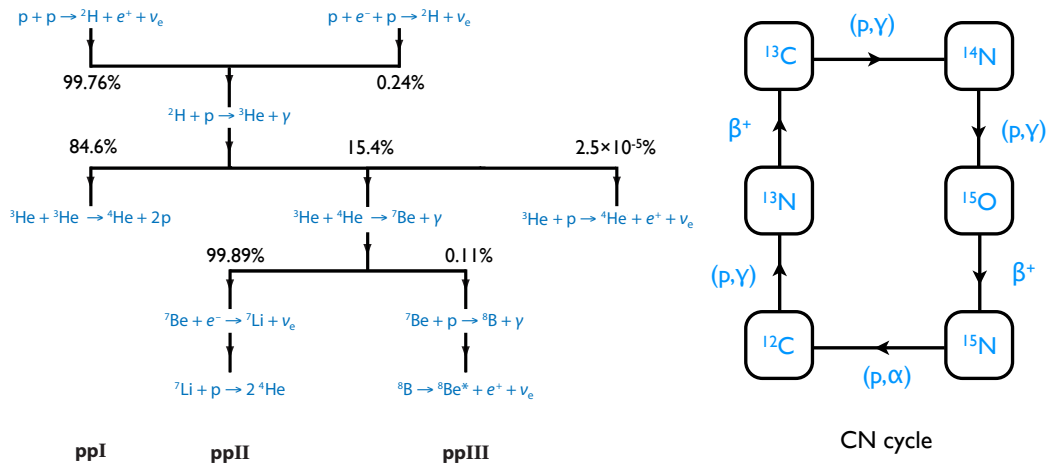


Figure 1: (Color online) The left frame shows the three principal cycles comprising the pp chain (ppI, ppII, and ppIII), the associated neutrinos that “tag” each of the three branches, and the theoretical branching percentages defining the relative rates of competing reactions (GS98-SFII SSM). Also shown is the minor branch ${}^3\text{He} + p \rightarrow {}^4\text{He} + e^+ + \nu_e$, which generates the most energetic neutrinos. The right frame shows the CN I cycle, which produces the ${}^{13}\text{N}$ and ${}^{15}\text{O}$ neutrinos.

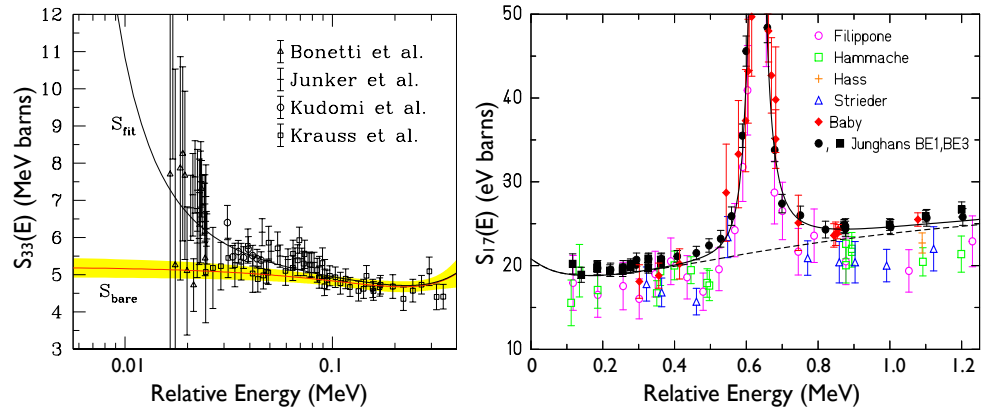


Figure 2: (Color online) Left panel: The data, the best quadratic+screening result for $S_{33}(E)$, and the deduced best quadratic fit (red line) and allowed range (yellow band) for S_{33}^{bare} . Right panel: $S_{17}(E)$ vs. center-of-mass energy E , for $E \leq 1250$ keV. Data points are shown with total errors, including systematic errors. The dashed line is based on a theoretical calculation, scaled to fit the data. See Solar Fusion II for references and details.

Table 2: SSM neutrino fluxes from the GS98-SFII and AGSS09-SFII SSMs, with associated uncertainties (averaging over asymmetric uncertainties). The solar values come from a luminosity-constrained analysis of all available data by the Borexino Collaboration.

ν flux	E_ν^{\max} (MeV)	GS98-SFII	AGSS09-SFII	Solar	units
$p+p \rightarrow {}^2\text{H}+e^++\nu$	0.42	$5.98(1 \pm 0.006)$	$6.03(1 \pm 0.006)$	$6.05(1^{+0.003}_{-0.011})$	$10^{10}/\text{cm}^2\text{s}$
$p+e^-+p \rightarrow {}^2\text{H}+\nu$	1.44	$1.44(1 \pm 0.012)$	$1.47(1 \pm 0.012)$	$1.46(1^{+0.010}_{-0.014})$	$10^8/\text{cm}^2\text{s}$
${}^7\text{Be}+e^- \rightarrow {}^7\text{Li}+\nu$	0.86 (90%) 0.38 (10%)	$5.00(1 \pm 0.07)$	$4.56(1 \pm 0.07)$	$4.82(1^{+0.05}_{-0.04})$	$10^9/\text{cm}^2\text{s}$
${}^8\text{B} \rightarrow {}^8\text{Be}+e^++\nu$	~ 15	$5.58(1 \pm 0.14)$	$4.59(1 \pm 0.14)$	$5.00(1 \pm 0.03)$	$10^6/\text{cm}^2\text{s}$
${}^3\text{He}+p \rightarrow {}^4\text{He}+e^++\nu$	18.77	$8.04(1 \pm 0.30)$	$8.31(1 \pm 0.30)$	—	$10^3/\text{cm}^2\text{s}$
${}^{13}\text{N} \rightarrow {}^{13}\text{C}+e^++\nu$	1.20	$2.96(1 \pm 0.14)$	$2.17(1 \pm 0.14)$	≤ 6.7	$10^8/\text{cm}^2\text{s}$
${}^{15}\text{O} \rightarrow {}^{15}\text{N}+e^++\nu$	1.73	$2.23(1 \pm 0.15)$	$1.56(1 \pm 0.15)$	≤ 3.2	$10^8/\text{cm}^2\text{s}$
${}^{17}\text{F} \rightarrow {}^{17}\text{O}+e^++\nu$	1.74	$5.52(1 \pm 0.17)$	$3.40(1 \pm 0.16)$	$\leq 59.$	$10^6/\text{cm}^2\text{s}$
χ^2/P^{agr}		3.5/90%	3.4/90%		

Table 3: Results from global 3ν analyses including data through Neutrino2012.

Parameter/hierarchy	Bari Analysis (Fogli et al. 2012)			Valencia Analysis (Forero, Tórtola & Valle 2012)		
	Best 1σ Fit	2σ Range	3σ Range	Best 1σ Fit	2σ Range	3σ Range
$\delta m_{21}^2 (10^{-5}\text{eV}^2)$	$7.54^{+0.26}_{-0.22}$	$7.15 \leftrightarrow 8.00$	$6.99 \leftrightarrow 8.18$	7.62 ± 0.19	$7.27 \leftrightarrow 8.01$	$7.12 \leftrightarrow 8.20$
$\delta m_{31}^2 (10^{-3}\text{eV}^2)$ NH	$2.47^{+0.06}_{-0.10}$	$2.31 \leftrightarrow 2.59$	$2.23 \leftrightarrow 2.66$	$2.55^{+0.06}_{-0.09}$	$2.38 \leftrightarrow 2.68$	$2.31 \leftrightarrow 2.74$
IH	$-(2.38^{+0.07}_{-0.11})$	$-(2.22 \leftrightarrow 2.49)$	$-(2.13 \leftrightarrow 2.57)$	$-(2.43^{+0.07}_{-0.06})$	$-(2.29 \leftrightarrow 2.58)$	$-(2.21 \leftrightarrow 2.64)$
$\sin^2 \theta_{12}$	$0.307^{+0.018}_{-0.016}$	$0.275 \leftrightarrow 0.342$	$0.259 \leftrightarrow 0.359$	$0.320^{+0.016}_{-0.017}$	$0.29 \leftrightarrow 0.35$	$0.27 \leftrightarrow 0.37$
$\sin^2 \theta_{23}$ NH	$0.386^{+0.024}_{-0.021}$	$0.348 \leftrightarrow 0.448$	$0.331 \leftrightarrow 0.637$	$\left\{ \begin{array}{l} 0.613^{+0.022}_{-0.040} \\ 0.427^{+0.034}_{-0.027} \end{array} \right.$	$0.38 \leftrightarrow 0.66$	$0.36 \leftrightarrow 0.68$
IH	$0.392^{+0.039}_{-0.022}$	$\left\{ \begin{array}{l} 0.353 \leftrightarrow 0.484 \\ 0.543 \leftrightarrow 0.641 \end{array} \right.$	$0.335 \leftrightarrow 0.663$		$0.600^{+0.026}_{-0.031}$	$0.39 \leftrightarrow 0.65$
$\sin^2 \theta_{13}$ NH	0.0241 ± 0.0025	$0.0193 \leftrightarrow 0.0290$	$0.0169 \leftrightarrow 0.0313$	$0.0246^{+0.0029}_{-0.0028}$	$0.019 \leftrightarrow 0.030$	$0.017 \leftrightarrow 0.033$
IH	$0.0244^{+0.0023}_{-0.0025}$	$0.0194 \leftrightarrow 0.0291$	$0.0171 \leftrightarrow 0.0315$	$0.0250^{+0.0026}_{-0.0027}$	$0.020 \leftrightarrow 0.030$	$0.017 \leftrightarrow 0.033$

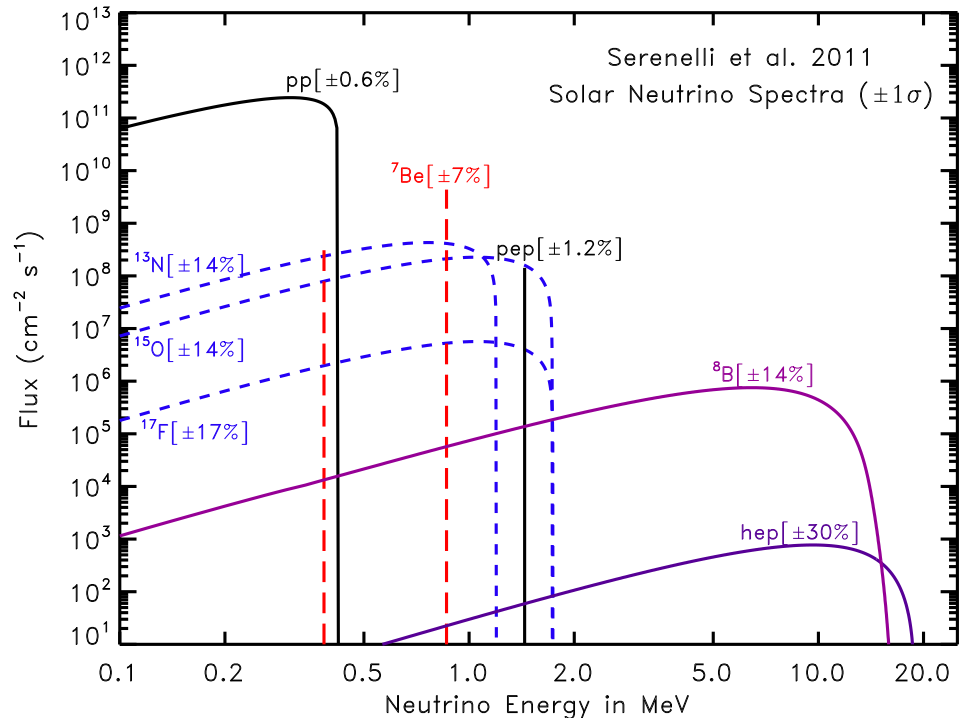


Figure 3: (Color online) The solar neutrino spectrum, along with the SSM uncertainties (Serrenelli, Haxton & Peña-Garay 2011). A weak branch from the β decay of ^{17}F that contributes from the CN II cycle is included. The units for the continuous sources are $\text{cm}^{-2} \text{s}^{-1} \text{MeV}^{-1}$.

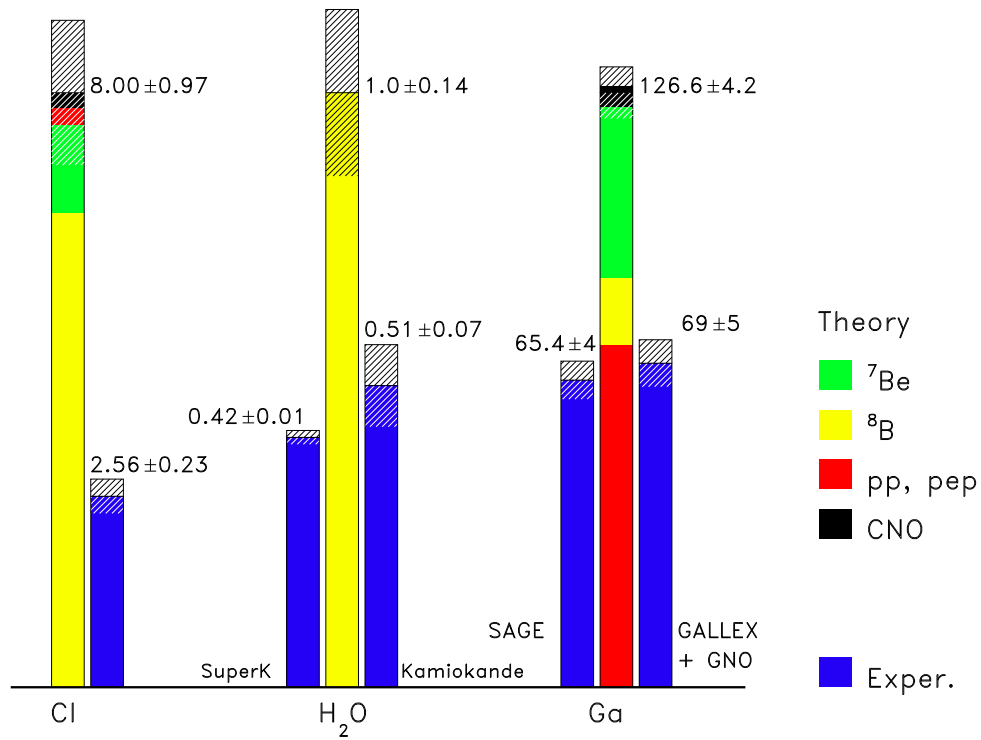


Figure 4: (Color online) Comparison of the measured neutrino rates for the chlorine, Kamioka II/III, and SAGE/GALLEX/GNO experiments with the contemporary SSM GS98-SFII, assuming unoscillated fluxes (Serenelli, Haxton & Peña-Garay 2011).

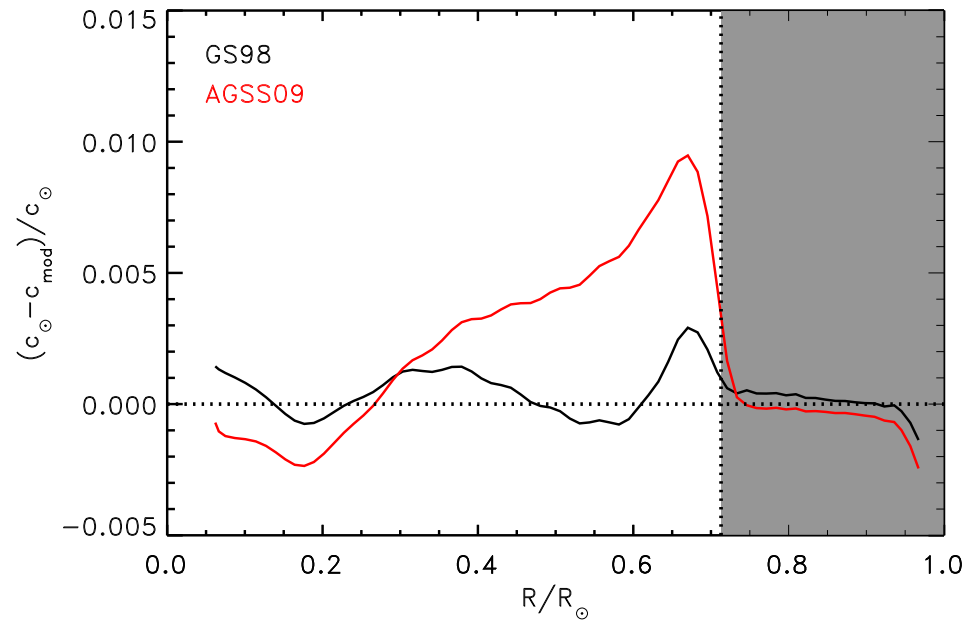


Figure 5: (Color online) The relative sound speed $(c(r)_{\text{solar}} - c(r)_{\text{SSM}}) / c(r)_{\text{SSM}}$ where $c(r)_{\text{SSM}}$ is the SSM result and $c(r)_{\text{solar}}$ the solar profile extracted from BiSON data. The black and red profiles correspond to the high-metallicity GS98-SFII and low-metallicity AGSS09-SFII SSMs, respectively.

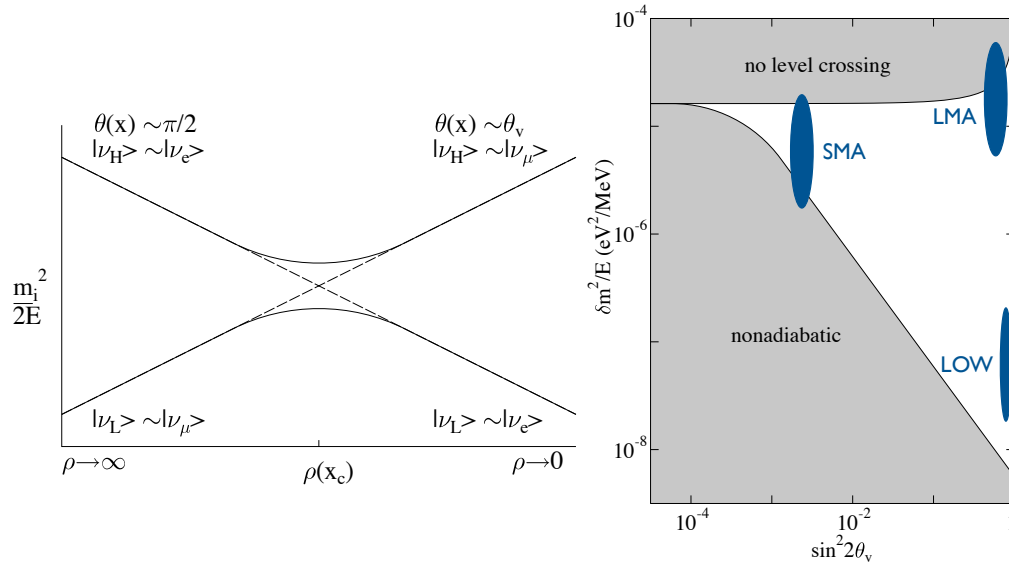


Figure 6: (Color online) Left: A schematic illustration of the MSW crossing for a normal hierarchy and small θ_ν . The dashed lines – the electron-electron and muon-muon diagonal elements of the m_ν^2 matrix – intersect at the level-crossing density ρ_c . The solid lines are the trajectories of the light and heavy local mass eigenstates. A ν_e produced at high density as $\sim \nu_H$ will, under adiabatic propagation, remain $\sim \nu_H$, exiting the Sun as $\sim \nu_\mu$. Right: the white “MSW triangle” is the region where a level crossing occurs and propagation is adiabatic, producing strong $\nu_e \rightarrow \nu_\mu$ conversion. Regions of three possible MSW solutions frequently discussed in the 1990s – SMA, LMA, and LOW – are depicted by the blue ellipses.

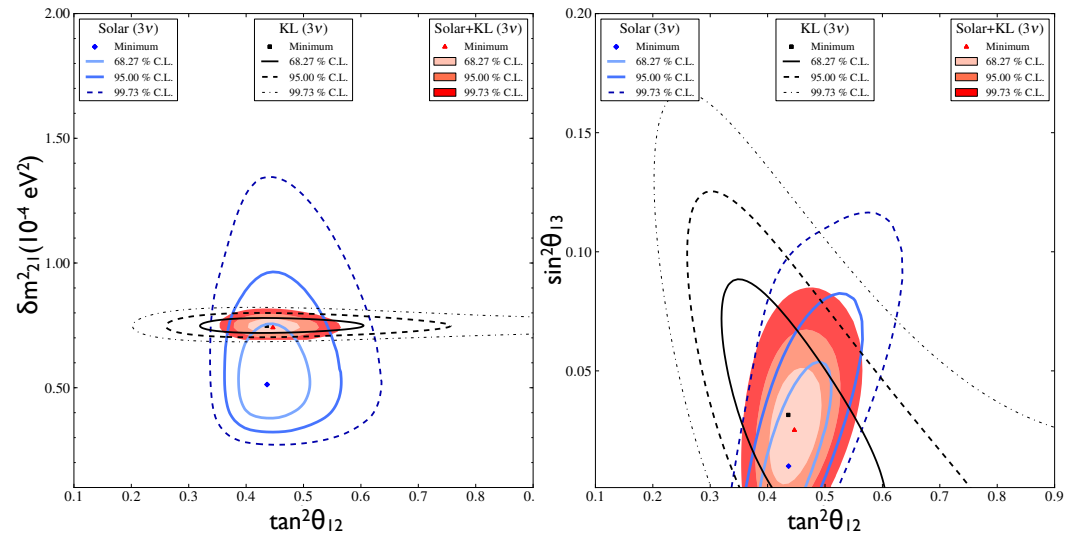


Figure 7: (Color online) The three-flavor neutrino oscillation contours resulting from the SNO combined analysis: the analysis employs only solar neutrino and KamLAND data, but the results are in excellent agreement with the conclusions from global analyses that include recent reactor- and accelerator-neutrino constraints on θ_{13} . From SNO Collaboration, B. Aharmim et al. (2012).

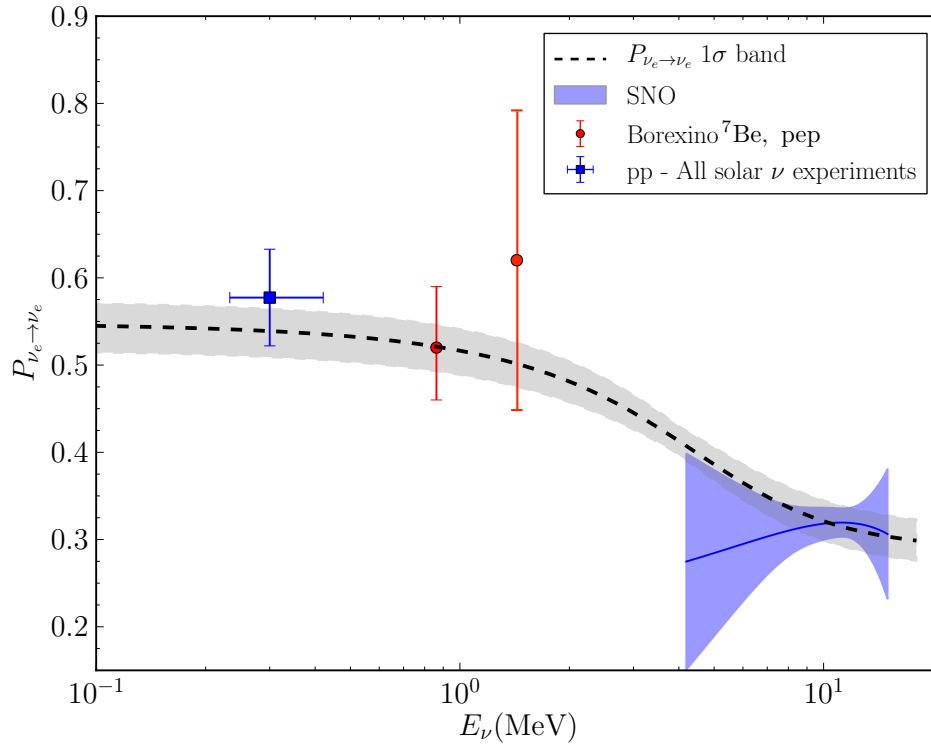


Figure 8: (Color online) Survival probabilities P_{ν_e} for pp, pep, ${}^7\text{Be}$, and ${}^8\text{B}$ neutrinos deduced from global solar neutrinos analyses, Borexino, and the SNO combined analysis, compared to the MSW prediction, taking into account present uncertainties on mixing angles. From SNO Collaboration, B. Aharmim et al. (2012), with pep result from Borexino Collaboration, G. Bellini et al. (2012a) added.

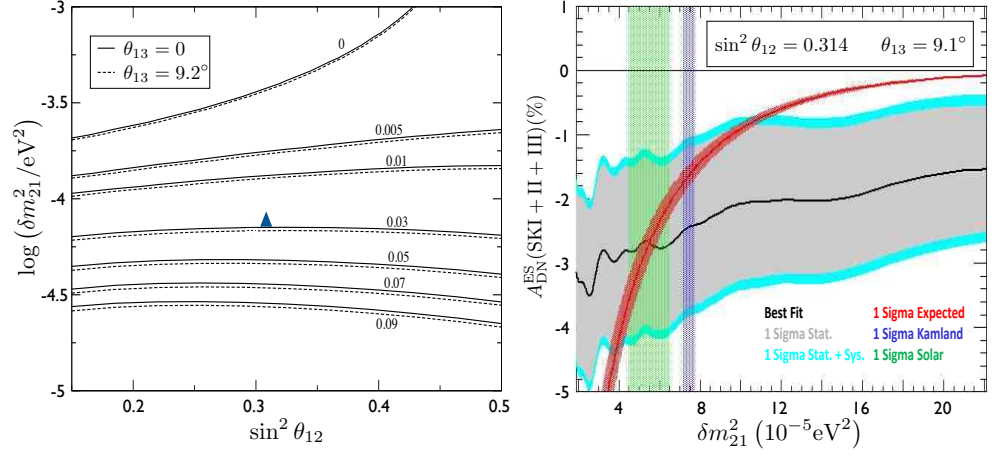


Figure 9: (Color online) Left panel: The expected $A_{\text{DN}}^{\text{ES}}$ for Super-Kamiokande as a function of δm_{21}^2 and $\sin^2 \theta_{12}$ for two (solid lines) and three (dashed lines, $\theta_{13} = 9.2^\circ$) flavors. The lines are the contours of constant $A_{\text{DN}}^{\text{ES}}$. The blue triangle marks the best-fit parameters from current global analyses. Adapted from Blennow, Ohlsson & Snellman (2004). Right panel: $A_{\text{DN}}^{\text{ES}}$ values consistent with current values of θ_{12} and θ_{13} (red band), plotted as a function of δm_{21}^2 , compared to SKI+II+III results (1σ statistical and statistical+systematic errors indicated). The vertical bands are the 1σ KamLAND and solar values for δm_{21}^2 . Adapted from A. Renshaw and M. Smy (private communication).

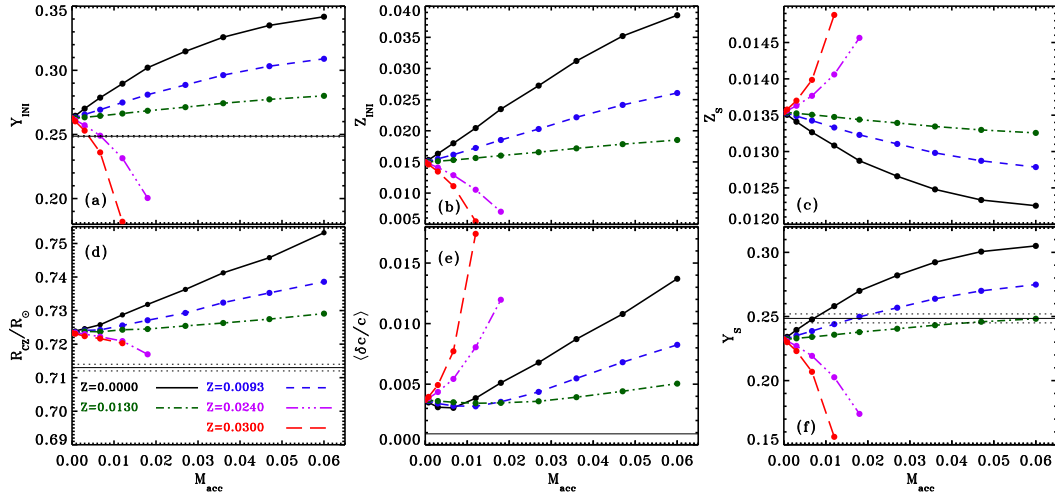


Figure 10: (Color online) Accretion on a young Sun with a thin convective envelope as a function of the mass and metallicity of the accreted material. The upper panels show the deduced He and metal content of the pre-solar gas, Y_{ini} and Z_{ini} , and present-day Z_S , determined from the luminosity, radius, and AGSS09 photospheric $Z_S/X_S=0.0178$ constraints. Truncated trajectories indicate the absence of a physical solution. The lower panels compare the resulting helioseismic properties of the models to observation (horizontal bands).

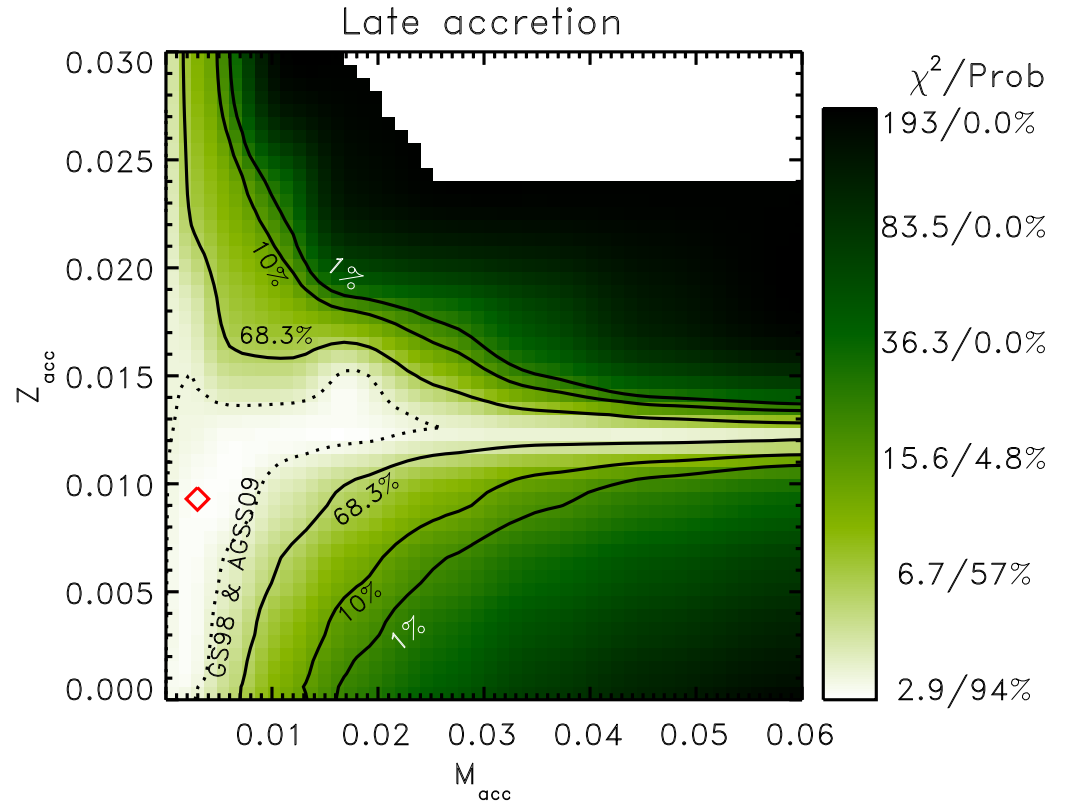


Figure 11: (Color online) Global χ^2 solar neutrino analysis for the late accretion NSSM scenario discussed in the text. Contours are shown for 1%, 10% and 68.4% confidence, with the best-fit model indicated by the red diamond. The fixed- χ^2 contours corresponding to the AGSS09-SFII and GS98-SFII SSM fits are overlaid, showing the very limited parameter space where NSSMs with accretion do better than SSMs.